



FALL/WINTER 2021 v13n2  
SPRING/SUMMER 2022 v14n1

Print ISSN: 2152-4157  
Online ISSN: 2152-4165

[WWW.IJERI.ORG](http://WWW.IJERI.ORG)

# International Journal of Engineering Research & Innovation

**Editor-in-Chief: Mark Rajai, Ph.D.**  
**California State University Northridge**



[www.ijeri.org](http://www.ijeri.org)

Print ISSN: 2152-4157  
Online ISSN: 2152-4165



[www.iajc.org](http://www.iajc.org)

# INTERNATIONAL JOURNAL OF ENGINEERING RESEARCH AND INNOVATION

## **ABOUT IJERI:**

- IJERI is the second official journal of the International Association of Journals and Conferences (IAJC).
- IJERI is a high-quality, independent journal steered by a distinguished board of directors and supported by an international review board representing many well-known universities, colleges, and corporations in the U.S. and abroad.
- IJERI has an impact factor of **1.58**, placing it among an elite group of most-cited engineering journals worldwide.

## **OTHER IAJC JOURNALS:**

- The International Journal of Modern Engineering (IJME)  
For more information visit [www.ijme.us](http://www.ijme.us)
- The Technology Interface International Journal (TIIJ)  
For more information visit [www.tiij.org](http://www.tiij.org)

## **IJERI SUBMISSIONS:**

- Manuscripts should be sent electronically to the manuscript editor, Dr. Philip Weinsier, at [philipw@bgsu.edu](mailto:philipw@bgsu.edu).

For submission guidelines visit  
[www.ijeri.org/submissions](http://www.ijeri.org/submissions)

## **TO JOIN THE REVIEW BOARD:**

- Contact the chair of the International Review Board, Dr. Philip Weinsier, at [philipw@bgsu.edu](mailto:philipw@bgsu.edu).

For more information visit  
[www.ijeri.org/editorial](http://www.ijeri.org/editorial)

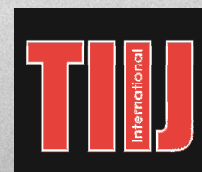
## **INDEXING ORGANIZATIONS:**

- IJERI is indexed by numerous agencies. For a complete listing, please visit us at [www.ijeri.org](http://www.ijeri.org).

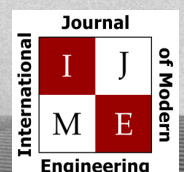
## **Contact us:**

**Mark Rajai, Ph.D.**

Editor-in-Chief  
California State University-Northridge  
College of Engineering and Computer Science  
Room: JD 4510  
Northridge, CA 91330  
Office: (818) 677-5003  
Email: [mrajai@csun.edu](mailto:mrajai@csun.edu)



[www.tiij.org](http://www.tiij.org)



[www.ijme.us](http://www.ijme.us)

---

# INTERNATIONAL JOURNAL OF ENGINEERING RESEARCH AND INNOVATION

The INTERNATIONAL JOURNAL OF ENGINEERING RESEARCH AND INNOVATION (IJERI) is an independent and not-for-profit publication, which aims to provide the engineering community with a resource and forum for scholarly expression and reflection.

IJERI is published twice annually (fall and spring issues) and includes peer-reviewed research articles, editorials, and commentary that contribute to our understanding of the issues, problems, and research associated with engineering and related fields. The journal encourages the submission of manuscripts from private, public, and academic sectors. The views expressed are those of the authors and do not necessarily reflect the opinions of the IJERI editors.

## EDITORIAL OFFICE:

Mark Rajai, Ph.D.  
Editor-in-Chief  
Office: (818)677-2167  
Email: [ijmeeditor@iajc.org](mailto:ijmeeditor@iajc.org)  
Dept. of Manufacturing Systems  
Engineering & Management  
California State University-  
Northridge  
18111 Nordhoff Street  
Northridge, CA 91330-8332

## THE INTERNATIONAL JOURNAL OF ENGINEERING RESEARCH AND INNOVATION EDITORS

### *Editor-in-Chief*

**Mark Rajai**

California State University-Northridge

### *Production Editor*

**Philip Weinsier**

Bowling Green State University-Firelands

### *Manuscript Editor*

**Philip Weinsier**

Bowling Green State University-Firelands

### *Subscription Editor*

**Morteza Sadat-Hossieny**

Northem Kentucky University

### *Publisher*

**Bowling Green State University-Firelands**

### *Web Administrator*

**Saeed Namyar**

Advanced Information Systems

### *Technical Editors*

**Andrea Ofori-Boadu**

North Carolina A&T State University

**Michelle Brodke**

Bowling Green State University-Firelands

**Marilyn Dyrud**

Oregon Institute of Technology

**Mandar Khanal**

Boise State University

**Chris Kluse**

Bowling Green State University

**Zhaochao Li**

Morehead State University

---

# TABLE OF CONTENTS

<i>Editor's Note: Registration is open for the 8<sup>th</sup> IAJC international conference in Orlando, Florida</i> .....	3
Philip Weinsier, IJERI Manuscript Editor	
<i>A Wireless Power-Consumption Measuring Device for Mobile Robots</i> .....	5
Flavio H. Cabrera, Pennsylvania State University - Berks	
<i>Plantar Pressure Monitoring System For Diabetic Feet</i> .....	13
Sanjeevi Chitikeshi, Old Dominion University; Aaron Isaac Kelman, Plasser American Corporation; Shirshak Dhali, Old Dominion University; Ajay Mahajan, University of Akron	
<i>Energy Consumption in Extrusion-Based Metal Additive Manufacturing</i> .....	20
Mehmet Emre Bahadir, Southeastern Louisiana University; Caleb Lagarrigue, PSX Worldwide Audiovisual Technologies; Juan Gonzalez, Pike Electric	
<i>Innovative Augmented Reality Application for Effective Utilization of Hazard Communication Pictograms</i> .....	29
Ulan Dakeev, Sam Houston State University; Ali Aljaroudi, Sam Houston State University	
<i>Difference in Response of a 40-Story, Buckling Restraint-Braced Frame Structure with Flexible Diaphragm</i> .....	33
Mohammad T. Bhuiyan, West Virginia State University	
<i>Instructions for Authors: Manuscript Formatting Requirements</i> .....	41



# 8<sup>TH</sup> IAJC INTERNATIONAL CONFERENCE

[www.2022.iajc.org](http://www.2022.iajc.org)

OCTOBER 13-16, 2022 – ORLANDO, FLORIDA

The leading indexed high-impact-factor conference on engineering and related technologies.

## Our Hotel—Embassy Suites



## Our Previous Tour—NASA's Kennedy Space Center



### CALL FOR CONFERENCE PROPOSALS

Conference Submission Deadlines:

- Abstract and Poster Submissions July 31, 2022
- Full-Paper Submissions (optional) July 31, 2022

Full papers may be submitted after a related abstract has been accepted for presentation. All full papers will automatically be reviewed for publication in the conference proceedings and the high-impact-factor IAJC journals after the conference. All submissions must be made using our online system at <https://2022.iajc.org/registration>

Have questions or need help? Contact Philip Weinsier (Conference General Chair) at [philipw@bgsu.edu](mailto:philipw@bgsu.edu)

## Editorial Review Board Members

Mohammed Abdallah	State University of New York (NY)	Rungun Nathan	Penn State Berks (PA)
Paul Akangah	North Carolina A&T State University (NC)	Arun Nambiar	California State University Fresno (CA)
Shah Alam	Texas A&M University-Kingsville (TX)	Aurenice Oliveira	Michigan Tech (MI)
Nasser Alaraje	Michigan Tech (MI)	Troy Ollison	University of Central Missouri (MO)
Ali Alavizadeh	Purdue University Northwest (IN)	Reynaldo Pablo	Purdue Fort Wayne (IN)
Lawal Anka	Zamfara AC Development (NIGERIA)	Basile Panoutsopoulos	Community College of Rhode Island (RI)
Jahangir Ansari	Virginia State University (VA)	Shahera Patel	Sardar Patel University (INDIA)
Sanjay Bagali	Acharya Institute of Technology (INDIA)	Thongchai Phairoh	Virginia State University (VA)
Kevin Berisso	Memphis University (TN)	Huyu Qu	Broadcom Corporation
Sylvia Bhattacharya	Kennesaw State University (GA)	Desire Rasolomampionona	Warsaw University of Tech (POLAND)
Monique Bracken	University of Arkansas Fort Smith (AR)	Michael Reynolds	University of West Florida (FL)
Tamer Breakah	Ball State University (IN)	Nina Robson	California State University-Fullerton (CA)
Michelle Brodke	Bowling Green State University (OH)	Marla Rogers	Fastboot Mobile, LLC
Shaobiao Cai	Minnesota State University (MN)	Dale Rowe	Brigham Young University (UT)
Rajab Chaloo	Texas A&M University Kingsville (TX)	Karen Ruggles	DeSales University (PA)
Isaac Chang	Illinois State University (IL)	Anca Sala	Baker College (MI)
Shu-Hui (Susan) Chang	Iowa State University (IA)	Alex Sergeev	Michigan Technological University (MI)
Rigoberto Chinchilla	Eastern Illinois University (IL)	Mehdi Shabanejad	Zagros Oil and Gas Company (IRAN)
Phil Cochrane	Indiana State University (IN)	Hiral Shah	St. Cloud State University (MN)
Curtis Cohenour	Ohio University (OH)	Mojtaba Shivaie	Shahrood University of Technology (IRAN)
Emily Crawford	Clafin University (SC)	Musibau Shofoluwe	North Carolina A&T State University (NC)
Dongyang (Sunny)Deng	North Carolina A&T State University (NC)	Jiahui Song	Wentworth Institute of Technology (MA)
Z. T. Deng	Alabama A&M University (AL)	Carl Spezia	Southern Illinois University (IL)
Sagar Deshpande	Ferris State University (MI)	Michelle Surerus	Ohio University (OH)
Marilyn Dyrud	Oregon Institute of Technology (OR)	Harold Terano	Camarines Sur Polytechnic (PHILIPPINES)
Mehran Elahi	Elizabeth City State University (NC)	Sanjay Tewari	Missouri University of Science & Techn (MO)
Ahmed Elsayy	Tennessee Technological University (TN)	Vassilios Tzouanas	University of Houston Downtown (TX)
Cindy English	Millersville University (PA)	Jeff Ulmer	University of Central Missouri (MO)
Ignatius Fomunung	University of Tennessee Chattanooga (TN)	Abraham Walton	University of South Florida Polytechnic (FL)
Ahmed Gawad	Zagazig University EGYPT)	Haoyu Wang	Central Connecticut State University (CT)
Hamed Guendouz	Yahia Farès University (ALGERIA)	Jyhwen Wang	Texas A&M University (TX)
Kevin Hall	Western Illinois University (IL)	Boonsap Witchayangkoon	Thammasat University (THAILAND)
Mohsen Hamidi	Utah Valley University (UT)	Shuju Wu	Central Connecticut State University (CT)
Mamoon Hammad	Abu Dhabi University (UAE)	Baijian "Justin" Yang	Purdue University (IN)
Gene Harding	Purdue Polytechnic (IN)	Xiaoli (Lucy) Yang	Purdue University Northwest (IN)
Bernd Haupt	Penn State University (PA)	Hao Yi	Chongqing University (CHINA)
Youcef Himri	Safety Engineer in Sonelgaz (ALGERIA)	Faruk Yildiz	Sam Houston State University (TX)
Delowar Hossain	City University of New York (NY)	Yuqiu You	Ohio University (OH)
Xiaobing Hou	Central Connecticut State University (CT)	Hong Yu	Fitchburg State University (MA)
Shelton Houston	University of Louisiana Lafayette (LA)	Pao-Chiang Yuan	Jackson State University (MS)
Ying Huang	North Dakota State University (ND)	Jinwen Zhu	Missouri Western State University (MO)
Christian Bock-Hyeng	North Carolina A&T University (NC)		
Pete Hylton	Indiana University Purdue (IN)		
John Irwin	Michigan Tech (MI)		
Toqeer Israr	Eastern Illinois University (IL)		
Alex Johnson	Millersville University (PA)		
Rex Kanu	Purdue Polytechnic (IN)		
Reza Karim	North Dakota State University (ND)		
Manish Kewalramani	Abu Dhabi University (UAE)		
Tae-Hoon Kim	Purdue University Northwest (IN)		
Chris Kluse	Bowling Green State University (OH)		
Doug Koch	Southeast Missouri State University (MO)		
Mohan Krishna	Vidyavardhaka College of Eng. (INDIA)		
Resmi Krishnankuttyrema	Bowling Green State University (OH)		
Zaki Kuruppalil	Ohio University (OH)		
Shiyoung Lee	Penn State University Berks (PA)		
Soo-Yen (Samson) Lee	Central Michigan University (MI)		
Chao Li	Florida A&M University (FL)		
Jiliang Li	Purdue University Northwest (IN)		
Zhaochao Li	Morehead State University (KY)		
Dale Litwhiler	Penn State University (PA)		
Lozano-Nieto	Penn State University (PA)		
Mani Manivannan	ARUP Corporation		
G.H. Massiha	University of Louisiana (LA)		
Thomas McDonald	University of Southern Indiana (IN)		
David Melton	Eastern Illinois University (IL)		
Shokoufeh Mirzaei	Cal State Poly Pomona (CA)		
Kay Rand Morgan	Mississippi State University (MS)		
Sam Mryyan	Excelsior College (NY)		
Jessica Murphy	Jackson State University (MS)		

# A WIRELESS POWER-CONSUMPTION MEASURING DEVICE FOR MOBILE ROBOTS

Flavio H. Cabrera, Pennsylvania State University - Berks

## Abstract

Measuring energy consumption is a primordial task in battery operated devices such as mobile robotic systems. Traditionally, energy measurements are done in controlled laboratory environments because of the need of using bench measurement equipment. But in real applications, real-time data collection is needed in order to observe the influence of the environment on the system's energy consumption. To achieve online data collection, user-modifiable, low-cost, small-footprint mobile measurement devices are needed. To date, measuring devices on the market have had several drawbacks, including proprietary technology not open to user modifications; dependency on additional equipment to be functional; or, a high market price that makes their use unattainable for large systems. In this paper, the authors presents a general purpose, low-cost, open-source, embedded measuring device that can be implemented and utilized by the robotics community at large. The results in terms of accuracy and precision of the implemented device are promising, and future improvements are discussed.

## Introduction

Energy is one of the main limiting factors when testing and deploying mobile robotic systems, and a key challenge of the SWaP (size, weight, and power) constraint discussed in many technological areas at this time. Out of this trifecta, the issue of power consumption and energy efficiency is the one that has received the least attention, due in part to the relatively low cost of rechargeable batteries, and to advances in smaller and lighter hardware. Despite this, the problem persists in applications where autonomy and payload are definitive. For example, typical deployment times for autonomous micro-UAVS is on the order of 10-20 minutes (Galkin, Kibilda, & Da Silva, 2019; Brommer, Maljuta, Hentzen, & Brockers, 2018).

The study of power use in mobile robotic systems requires the precise measurement of electric current and voltage on a diverse type of elements (motors, controllers, sensors, and other actuators). Also, to calculate energy consumption in real time, data logging and processing are required. An additional challenge with mobile robots is their obvious mobile nature. As such, for mobile robotic systems, the most appropriate way to measure energy consumption is by doing it while they are moving in a real environment. Considering that mobile robotics encompasses not only terrestrial (wheeled) robots but also aerial and aquatic ones, a power measuring device must have additional characteristics beyond accuracy. It must be small in size, light in

weight, adaptable to energy measurement in different elements within the system (individual sensors, motors, controllers, etc.), capable of logging/processing/transmitting the data while consuming the least amount of energy (preventing it from becoming a burden to the system), and have a low cost of production (an important feature when dealing with multi-robot systems). To the best of the author's knowledge, such a tool does not exist. The author acknowledges the commercial availability of small current sensors such as Adafruit's INA219 (Adafruit, 2021) or Allegro MicroSystems' ACS712 (Allegro, 2021) or of energy modules such as Maxim's MAX44299 (Maxim, 2020), but their integration into a workable measuring device with the aforementioned functionality requires additional hardware that makes this work more than compelling.

The aim of this paper is to introduce the design and implementation of a general purpose, low-cost, open-source, embedded measuring device that can be implemented and utilized by the robotics community. The design considers connection interfaces that can be connected to different elements within a robotic system, making it ideal for measuring power consumption in individual elements as well as the whole system. The advantages of utilizing this measuring device are: i) low-cost of production; ii) low energy consumption; iii) allows for consistent measurements among different devices and peripherals; and, iv) allows for benchmarking among different systems and algorithms. Moreover, the open-source nature of this project makes possible the collaborative effort of the whole robotics community to improve the device.

## Background

The study of how different components of a mobile robot system consume electric power has prompted most researchers to classify them in three broad categories: the motion system (motors and actuators), the sensor system (all sensor data acquisition units), and the control system (embedded microcontrollers and hardware related to the processing of control algorithms) (Hou, Zhang, & Kim, 2019; Mei, Lu, Hu, & Lee, 2004). But determining which consume the most power is in many cases left to intuition. For example, traditionally it has been believed that out of the three, the motion system is the one that consumes more power (Mei, Lu, Hu, & Lee, 2006; Wang, Yang, & Li, 2013). But as stated in a study by Zorbas and Razafindralambo (2015), in some cases, the control system may surpass the power consumption of the motors. There is no clear understanding either in how, during robot operation, the energy is consumed over time. Understanding the

---

latter may allow for the improvement of energy consumption by changing the way that certain tasks are performed, or the way certain peripherals/sensors are used.

To date, most studies on energy consumption have been focused on two aspects. First, creating models in order to predict energy consumption on the three aforementioned categories (Mei, Lu, Hu, & Lee, 2005); or in specific types of mobile robots (Xiao & Whittaker, 2014; Wahab, Rios-Gutierrez, & Shahat, 2015); or in specific elements, such as motors, within the robotic system (Kim & Kim, 2007; Trzynadlowski, 1988). Second, defining control algorithms for optimal motion or path planning (Liu & Sun, 2014; Mei et al., 2005; H. Kim & Kim, 2008; Bartlett, Gurau, Marchegiani, & Posner, 2016) to extend overall battery life. For many of these studies, measuring energy consumption was performed as a means to validate results, but few insights were given in terms of how it was done. In some cases, the estimation of power consumption was done indirectly by measuring the time the robots were capable of performing a task between charges (Krintz, Wen, & Wolski, 2004). In such instances, the Smart Battery System (SBS) presented in rechargeable batteries has been used to monitor the battery status. It has become widely used because no modification to the system is required and estimated measurement of voltage level can be obtained by invoking software functions. For example, Narayanan (2005) estimated power consumption by using statistics of device states and activity of the system. The drawback of this approach is that it does not allow for obtaining a per-device power consumption measurement.

It is worth noting that several mobile robots have integrated power measuring devices. For example, on Intel Aero platforms (Intel, 2020), there is one integrated Intel power management unit that can measure overall system power consumption. However, this power management unit is not open for end-user utilization and its documentation is not open to the public either. Another limitation is that it cannot handle voltages higher than 5V, which means it could not measure the battery voltage properly without additional modifications. Consequently, the first step in dealing with energy consumption and efficiency in mobile robots is to be able to measure it consistently during execution time. Traditional ways of measuring energy consumption consider the use of dedicated bench equipment in a controlled laboratory setting. This approach has been used in mobile robotic systems for testing of consumption models (Hou et al., 2019), but the bulkiness of the equipment makes it rather impractical for realistic scenarios and could yield results that do not reflect the actual energy consumption of the robots once they move in a non-controlled environment (Zorbas & Razafindralambo, 2015; Xiao & Whittaker, 2014).

Several other approaches, more suitable for mobile robotics, have been considered with different types of equipment and different purposes in mind. For example, Mei et al. (2005) used a digital acquisition board along with laptop

computers placed on top or near the mobile robot to measure the overall power consumption of a wheeled robot; Wahab et al. (2015) used an ACS712 current sensor paired with an Arduino Mega 2560 to collect the electric current passing through the motors of a differential drive wheeled robot; Tokekar, Kamad, and Isler (2011) used an Attopilot voltage and current measurement circuit from SparkFun Electronics to measure the current and voltage utilized by the two motors of their mobile wheeled platform, but no additional details of the measurement equipment were provided. Abeywickrama, Jayawickrama, He, and Dutkiewicz (2018) considered the use of commercially available, general-purpose meters to measure power consumption of UAVs. The data were then used to create a model of the power consumption in the flying robot. In many other studies in literature, such as Liu and Sun (2014) and Bartlett et al. (2016), the utilization of voltage and current sensors for measuring consumed power was mentioned, but no description of the setup or the data collection parameters were given. The authors used these unspecified measuring devices to measure power consumption of motors using different sampling rates and voltages with the purpose of modeling power consumption either of the motors or the overall system.

From these studies and others in the literature, it is noticeable that the tool to measure energy consumption is consistently different. Also, given the fact that energy consumption and efficiency in mobile robots is at the center of many research projects, the lack of a consistent measuring tool is appalling, a fact that was asserted by Abeywickrama et al. (2018). Furthermore, although the methodology to measure energy consumption is very important (Nakutis, 2009; Haulin, 2018), it is seldom considered or mentioned in the literature about energy studies on mobile robots.

## System Design

In this current study, the author proposed an embedded mobile power measuring device formed by three different sub-systems for measuring, processing, and communication. At a practical level, measuring energy consumption is based on the ability to measure the two basic electric circuit variables (current and voltage) over a period of time. In most cases, the assumption is that the voltage utilized by a system is constant. As such, the challenge becomes one of accurately measuring electric current. There are several ways to measure electric current.

1. The current mirror method, which consists of a circuit typically formed by at least two cascaded transistors. Due to the arrangement of the transistors, the output current mirrors the value of the input (the current to be measured), while providing a high output impedance that makes the reading insensitive to the impedance of the output load (Gray, Hurst, Lewis, & Meyer, 2009). Not exclusively used for current measurement, it has been used for this purpose in other studies to measure how software-related tasks consume power at the instruction level in embedded systems (Konstantakos &

Laopoulos, 2006; Nikolaidis & Laopoulos, 2001; Laopoulos, Neofotistos, Kosmatopoulos, & Nikolaidis, 2003; Borovyi, Kochan, Sachenko, Konstantakos, & Yaskilka, 2007; Kavvadias, Neofotistos, Nikolaidis, Kosmatopoulos, & Laopoulos, 2004).

2. The charge transfer method considers the use of a known capacitor that is charged either by the power supply or by the current consumed by the load. In the former, the capacitor is discharged by the load and the remaining voltage indicates how much current was consumed (Chang, Kim, & Lee, 2002). In the latter, the discharging time indicates how much current was used to charge the capacitor (Konstantakos, Kosmatopoulos, Nikolaidis, & Laopoulos, 2006).
3. The magnetic coupling method utilized in current probes is a well-used method for measuring high currents, because the circuit does not need to be intervened to collect data. The method, however, is less used in small DC current circuitry, in part due to limited accuracy of the readings and the high cost of these probes (Asahi, 2021).
4. A more novel approach to measuring current is the thermal monitoring method (Wolf, Kruse, & Ernst, 2002). The method uses integrated software to estimate the temperature of a processor, and it is based on existing models relating the thermal profile of a chip processor with the amount of leakage current that it exhibits. Although it has good accuracy (3.5% or better), it is not intended for dynamic estimation of power consumption, and it is limited to measuring small currents such as those due to leakage or while the processor is in the sleep mode.
5. The simplest and most popular way to measure current, however, is the current shunt method. It measures the voltage drop across a small (shunt) resistor that is inserted in series with the power line, either between the source and the load or between the load and the common ground. Since the shunt resistor is connected in series, and to prevent a significant voltage drop to occur across it, its value is small (typically on the order of m $\Omega$ ). The voltage value is then read by using either an analog or a digital transducer. In the case of a digital transducer, the signal passes first through an analog-to-digital converter (ADC) and then the values are inputted into the digital processor. In most cases, the signal is passed through an operational amplifier (or op amp) before passing through the ADC.

All of these different methods have advantages and disadvantages, depending on the application. In most cases, the methods are combined: for example, the current mirror and charge transfer methods are often used to condition the current, which is then passed through a shunt resistor to actually perform the measurement. In terms of accuracy, the current mirror method is regarded as capable of providing a high accuracy, but with the caveat that it needs to be carefully tweaked so as to prevent noise in the circuit or distortion due to poorly matched transistors.

For a mobile measuring device like the one proposed in this current study, simplicity is key to making it implementable in a reduced space and with the lowest possible footprint (lightweight and with low power consumption). In this project, the current shunt method, based on the design by Jones (2009) was used. Figure 1 shows a schematic of the circuit.

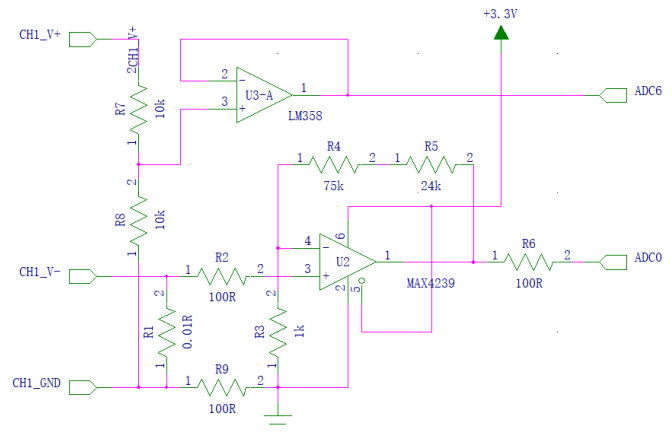


Figure 1. Schematic of measuring channel.

As shown, it considers the use of two op amps: one is used as a buffer for sending the voltage signal to the ADC unit for measuring, while the second one is used to condition the current signal from the shunt resistor before being sent to the processing unit. The voltage follower is obtained by means of an LM358 general purpose, low voltage op amp. The conditioning of the current signal is done through an MAX4239 ultra-low offset, precision amplifier connected in a noninverting amplifier configuration.

The design took into account the use of a 0.01 $\Omega$  shunt resistor suitable for measuring currents in the 1mA to 3A range. Future modifications of the circuit could include additional shunt resistors to capture smaller currents in the  $\mu$ A and nA ranges. The current circuit also took into account three points of connection: one for the voltage terminal and two for the return of the current being measured. The measuring system was required to be powered by an external voltage source in the range of 3-5V. The concept of operation is simple: the current from the circuit flows through the shunt resistor, producing a small voltage drop, which is then amplified by the op amp. The gain of the amplifier is defined by resistors R3, R4, and R5, which are set to produce a gain of 100.

In order to make it into an embedded device, a microcontroller was used to take the samples of voltage and current and process them into measurements of power: the LPC54102 microcontroller from NXP semiconductors was used. This is a 32-bit, 64-pin, dual core, low-power microcontroller based on ARM(R) Cortex-M architecture. It has a total of twelve 12-bit analog-to-digital converter (ADC)

channels, supporting up to 5M samples/s, with dual independent conversion sequences. When working at its maximum clock frequency of 150 MHz, it consumes a maximum of 150mW at 60mA. Figure 2 shows the connections made for the LPC54102 within the circuit. In this project, both cores were used simultaneously: one for measuring the voltage and current and one for averaging and summing the current in the calculation of power. The second core was also responsible for sending data wirelessly to an external computer for plotting and data logging.

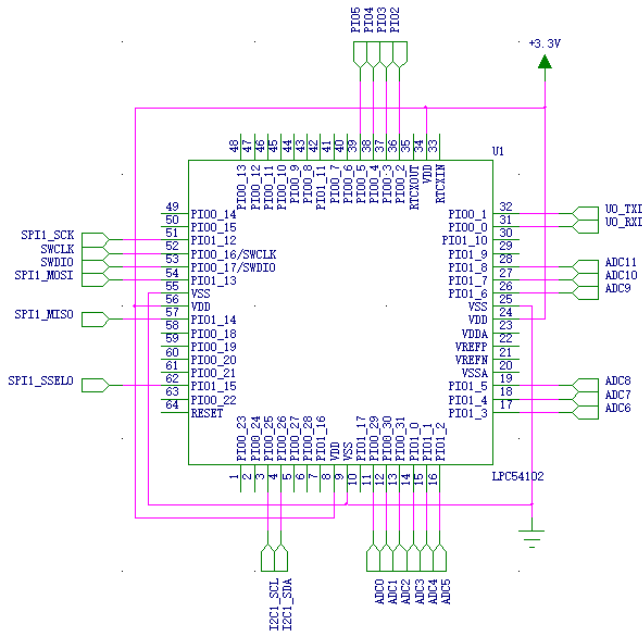


Figure 2. Connection pins for the LPC54102 MCU.

Due to the mobile nature of this measuring device and to the limited on-chip memory (512kB) of the LPC54102, data logging was done on an external computer. As such, wireless communication was essential for this application. The Espressif's ESP8266 wireless controller within an ESP-01 Wi-Fi module by Ai-Thinker Technology Company was used. The controller is compliant with 802.11b/g/n wireless LAN protocol, with integrated full TCP/IP protocol stack and adopted the standard AT command protocol, which greatly simplify the design of user applications (Espressif, 2020). This module contains a 32-bit ARM processor, with 1MB of flash memory, a 10-bit ADC, and 2 GPIOs that can be used as a serial-to-Wi-Fi bridge (as used in this current project), or as a standalone processing unit.

Figure 3 shows the wireless module that, when working at 3.3V and draws an average of 170mA/140mA when transmitting on 802.11b/g channels, making it the highest power drawing element in the entire design (560-460mW). As a result, and to maintain its low-footprint characteristics (weight-wise), the measuring device needed to be powered by the battery of the mobile robot. An aspect for future de-

velopment is to make the measuring device completely self-powered and independent from the system it is trying to measure.

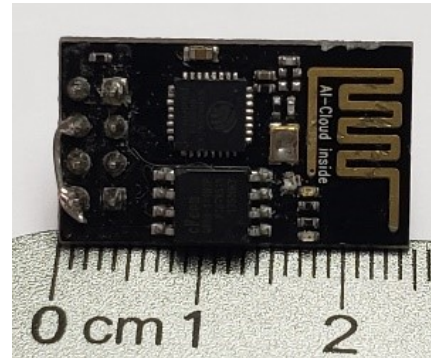


Figure 3. Wireless module ESP-01.

To integrate the wireless module into the system, the microcontroller would first wait for the wireless module controller to start up, then command it to set up a Wi-Fi access point and a TCP server. During normal operation, an external computer would be connected to this TCP server and the microcontroller would send data to the first active client connected to the TCP server. It is worth mentioning that the ESP-01 board can accept more than one client connected at a time, but for the operation of this embedded device, data were sent only to the first active one.

## Data Plotting and Logging

As mentioned earlier, this design took data logging into consideration; plotting was done on an external computer. Receiving data from the measuring unit was done via wireless communication through a client application in the receiving computer. This client was coded in Python and was capable of both plotting and logging the data. It utilized the "matplotlib" library, which offered plotting functions similar to those of higher-end software such as MATLAB. Other necessary functions were already provided by the Python standard library. The operation of the client application tried first to connect to the TCP server hosted by the embedded measuring device. If successful, it would continuously receive data from the server, plot them on the screen, and store them on the hard drive for future reference.

## Hardware Implementation

Figure 4 shows the embedded measuring device, which was implemented on an 8-by-3 cm circuit board with all of the components placed on one side of the board, except for a DF12 receptacle for board-to-board connection. Figure 5 shows that the size and weight of board was about 4 grams; thus, the impact of the proposed measuring device when attached to a mobile robot or aerial vehicle was almost negligible.

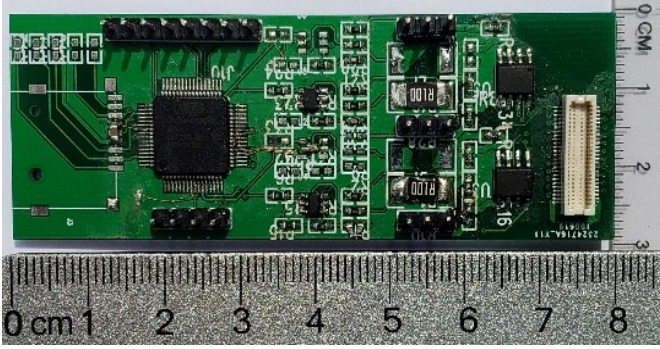


Figure 4. Dimensions of the measuring device.



Figure 5. Weight of the measuring device.

Due to the capabilities of the microprocessor (12 ADC channels and dual simultaneous conversion) and of the op amps, it was possible to include more than one measuring channel per board. As such, in the 8-by-3 board used in this project, it was possible to accommodate four measuring channels, although the author chose to fully implement only two. Figure 6 shows that the interfacing of the board was mainly done through pin headers. The microcontroller was programmed through header J10. Header J1 was used to power the measuring device and for connecting the wireless module ESP-01.

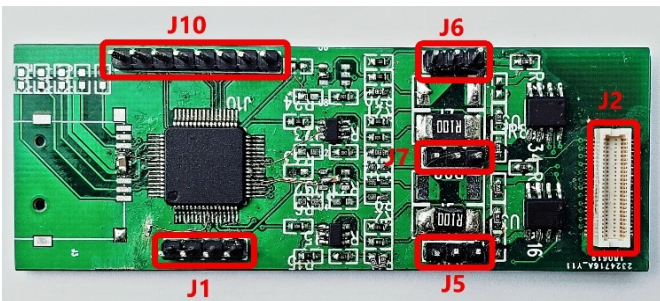


Figure 6. Interfacing connectors.

Each measuring channel had dedicated input connectors. Three of them used pin headers—J5, J6, and J7—to interface with the testing circuit. The fourth measuring channel utilized a DF12 board-to-board connector (J2). The fully

implemented channels were at headers J5 and J7. As observed, the design offered ample space for incorporating additional features in the future. As noted previously, each measuring channel used three pins, and each channel collected measurements of voltage and current. Figure 7 shows the required connections for the circuit under test.

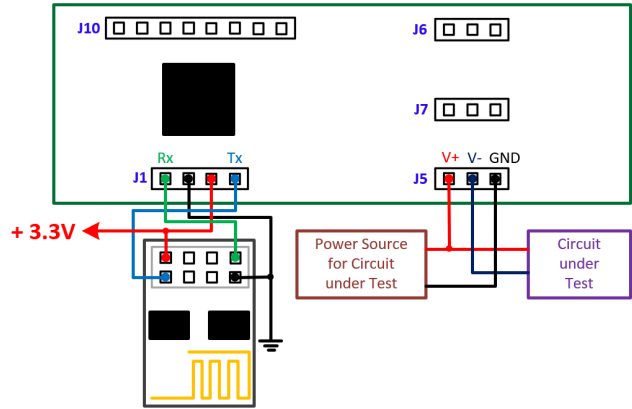


Figure 7. Connection to the testing circuit and the Wi-Fi module.

The design blueprints and programming files for the microcontroller and the client have been made available for public use in a GitHub repository (<https://github.com/fhcabrera/EnergyMeasuringDevice>). The use of the materials on this repository are subject to the GNU General Public License. As such, and in accordance with the main objective of this project, any modifications or improvements to the measurement device should remain available to the larger research community.

## Results

Accuracy is a key parameter when dealing with measuring devices. To test for accuracy, the measurements of voltage and current done with this embedded measuring device were compared with those done with a calibrated workbench multimeter (Keithley 2110). A calibrated power supply (BK-Precision 1710A) was used to produce a constant voltage (when testing for voltage accuracy) and a constant current (when testing for current accuracy). The voltage (and current) was then measured with both the workbench multimeter and the embedded measuring device. Tables 1 and 2 shows the results of the set of 10 measurements per each value that were collected and averaged. The embedded measuring device was powered using a second power supply. Table 1 shows the DC accuracy of DC voltage sensing, while Table 2 shows the accuracy of DC current sensing.

It was observed that variation in precision per each set of 10 measurements was negligible. For a measuring device, linearity is an indicator of consistency of its measurements. In other words, it indicates how well the device responds to changes in the measured quantity. To test for linearity, a linear regression was performed, calculating the  $R^2$  over the

collected data. The results showed an  $R^2$  of 0.999972 for current measurements and 0.999385 for voltage measurements. This indicates that the collected data were very close to the linear regression and that the measuring device was consistent in its readings. Also observed was a significant zero offset in the current measurement. This was expected, since a dual supply voltage for the MAX4239 op amp was not used.

Table 1. Accuracy of DC voltage measurement.

Voltage (V)	Embedded Device Reading (V)	Workbench Multi-meter Reading (V)	Error (%)
0.1	0.0976	0.0999	2.3023
0.2	0.1984	0.2000	0.8000
0.3	0.2972	0.2998	0.8672
0.4	0.3974	0.4000	0.6500
0.5	0.4985	0.5000	0.3000
0.6	0.6005	0.5998	0.1167
0.7	0.7032	0.6994	0.5433

Table 2. Accuracy of DC current measurement.

Current (A)	Embedded Device Reading (A)	Workbench Multi-meter Reading (A)	Error (%)
0.2	0.2168	0.1960	10.6122
0.5	0.5386	0.5000	7.7200
1.0	0.9524	0.9970	4.4734
2.0	1.8704	2.0010	6.5267
3.0	2.947	2.9990	1.7339
4.0	4.1061	3.9980	2.7039
5.0	4.9955	5.0010	0.1100

The testing for voltage readings was purposely constrained to small voltage values (in the range 0.1-0.7V) in order to observe the handling of such small quantities by the device. Figure 8 shows how a second test was done by connecting the embedded measuring device to the Raspberry Pi processing board in a TurtleBot 3 Burger robot platform (Robotis, 2020). The goal was to observe the capability of this measuring device for detecting fast and small changes in current consumption, as well the capability of the system to collect and plot this kind of data. To this end, data were collected at the booting up process of the Raspberry Pi board in the drone. Figure 9 shows the results of this test.

## Future Work

The design presented in this paper has room for improvement, and additional adjustments can be included, depend-

ing on individual measurement requirements. For example, a key improvement would be the inclusion of a virtual ground (by means of a third operational amplifier per channel). The virtual ground concept is an important one when dealing with mobile devices, since it serves as a steady reference point for the measurements of both voltage and current in the circuit. It also allows for the use of a single voltage source to serve as a double rail circuit that includes op amps.

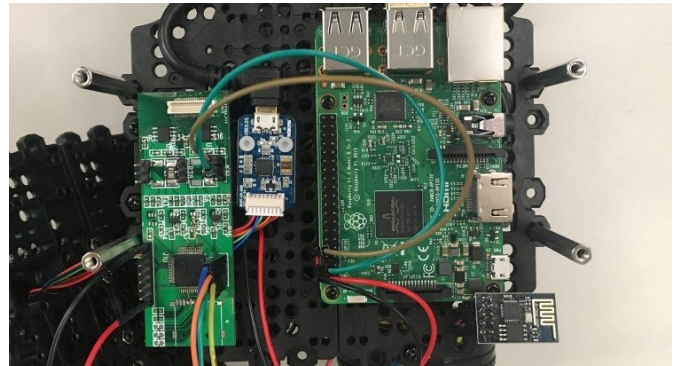


Figure 8. Measuring device on the Raspberry Pi board on a TurtleBot 3 robot.

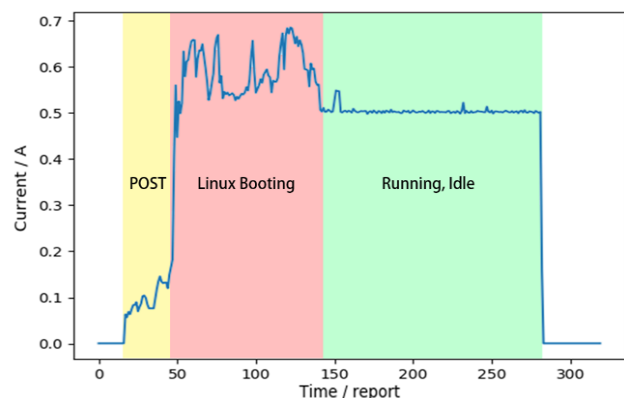


Figure 9. Current consumption of the Raspberry Pi at boot-up.

Another improvement could be to make the measuring device self-powered. This will free the measuring device from latching onto the power source of the circuit from which it is trying to measure. The main obstacle in achieving this second improvement is the Wi-Fi module. As described earlier, the Wi-Fi module is the element that consumes by far the most power on the device. Thus, a self-powered measuring device could be attainable by including data logging within the measuring device itself, alleviating the need for a Wi-Fi module. A third improvement involves the inclusion of additional shunt resistors that will allow for measuring currents in the range of  $\mu\text{A}$  and  $\text{nA}$ . In terms of software, the data logging client application was originally coded in Python, due to its simplicity. But simplicity comes at the price of performance. The use of "matplotlib" for

online plotting does not run well on mobile devices, such as tablets, and the report rate for the application must be reduced in order for the client to keep up. The use of a more robust programming language such as C may improve the efficiency of the client.

## Conclusions

In this paper, the author presented the design and implementation of a low-cost, open-source, embedded power consumption measuring device that can be used in applications that require mobility and a small footprint. Preliminary results for such a device are promising. The embedded measuring device used operational amplifiers to condition the voltage and current signals, a low-power microcontroller, and a Wi-Fi module to send data to an external computer for data logging. The measured data were compared to that of workbench equipment and showed a sufficient degree of accuracy. The measurement device was far from perfect, and there were different areas in which it could be further developed and improved. However, the author feels that it serves as a good starting point for an open-source development of small measuring devices.

## Acknowledgments

The work presented in this paper was supported by the PSU Research Development Grant Program through grant RDG 260-04 BK. The Author would like to thank Mr. Wenting Zhang for his help in developing hardware and software for this project. Mr. Zhang was, at the time of this project, a second-year student in the electrical engineering and computer science programs at Penn State University.

## References

- Abeywickrama, H. V., Jayawickrama, B. A., He, Y., & Dutkiewicz, E. (2018). Empirical power consumption model for UAVs. Paper presented at the IEEE vehicular technology conference (VTC), Chicago, IL, 27-30 August (pp. 1-5).
- Allegro Microsystems. (2021). *ACS712: Fully integrated, hall-effect-based linear current sensor*. Retrieved from <https://www.allegromicro.com/en/Products/Sense/Current-Sensor-ICs/Zero-To-Fifty-Amp-Integrated-Conductor-Sensor-ICs/ACS712>
- Asahi Kasei Microdevices. (2021). *Types and Characteristics of Current Sensors*. Retrieved from <https://www.akm.com/us/en/products/current-sensor/tutorial/types-characteristics/>
- Bartlett, O., Gurau, C., Marchegiani, L., & Posner, I. (2016). Enabling intelligent energy management for robots using publicly available maps. Paper presented at the IEEE international conference on intelligent robots and systems (IROS), Daejeon, South Korea, 9-14 October (pp. 2224-2229).
- Borovy, A., Kochan, V., Sachenko, A., Konstantakos, V., & Yaskilka, V. (2007). Analysis of circuits for measurement of energy of processing units. Paper presented at the 4th IEEE workshop on intelligent data acquisition and advanced computing systems: Technology and applications (IDAACS), Dortmund, Germany, 6-8 September (pp. 42-46).
- Brommer, C., Maljuta, D., Hentzen, D., & Brockers, R. (2018). Long-duration autonomy for small rotorcraft UAS including recharging. Paper presented at the 2018 IEEE/RSJ international conference on intelligent robots and systems (IROS), Madrid, Spain, 1-5 October (pp. 7252-7258).
- Chang, N., Kim, K., & Lee, H. G. (2002). Cycle-accurate energy measurement and characterization with a case study of the am7tdmi. *IEEE Transactions on Very Large Scale Integration (VLSI) Systems*, 10(2), 146-154.
- Espressif Systems. (2020). ESP8266EX data sheet. (Version 6.4). Espressif Systems.
- Galkin, B., Kibilda, J., & DaSilva, L. (2019). UAVs as mobile infrastructure: Addressing battery lifetime. *IEEE Communications Magazine*, 57, 132-137.
- Gray, P. R., Hurst, P. J., Lewis, S. H., & Meyer, R. G. (2009). *Analysis and design of analog integrated circuits*. Wiley.
- Haulin, L. (2018). *A state-based method to model and analyze the power consumption of embedded systems* (Independent thesis advanced level, Uppsala University). URN: <urn:nbn:se:uu:diva-363330>
- Hou, L., Zhang, L., & Kim, J. (2019). Energy modeling and power measurement for mobile robots. *Energies*, 12(1). doi: 10.3390/en12010027.
- Adafruit. (2021). *INA219 high side dc current sensor*. Retrieved from <https://learn.adafruit.com/adafruit-ina219-current-sensor-breakout>
- Intel. (2020). Intel Aero ready to fly drone. Retrieved from <https://www.intel.com/content/www/us/en/support/products/98471/drones/development-drones/intel-aero-products/intel-aero-ready-to-fly-drone.html>
- Jones, D. L. (2009). The  $\mu$ current a professional precision current adapter for multimeters. *Silicon Chip Magazine*, 58-65.
- Kavvadias, N., Neofotistos, P., Nikolaidis, S., Kosmatopoulos, C., & Laopoulos, T. (2004). Measurements analysis of the software-related power consumption in microprocessors. *IEEE Transactions on Instrumentation and Measurement*, 53(4), 1106-1112.
- Kim, C. H., & Kim, B. K. (2007). Minimum-energy translational trajectory generation for differential-driven wheeled mobile robots. *Journal of Intelligent and Robotic Systems*, 49, 367-383.
- Kim, H., & Kim, B. K. (2008). Minimum-energy translational trajectory planning for battery-powered three-wheeled omni-directional mobile robots. Paper presented at the 10th International conference on control, automation, robotics and vision (ICARCV), Hanoi, Vietnam, 2-5 December (pp. 1730-1735).

- Konstantakos, V., Kosmatopoulos, K., Nikolaïdis, S., & Laopoulos, T. (2006). Measurement of power consumption in digital systems. *IEEE Transactions on Instrumentation and Measurement*, 55(5), 1662-1670.
- Konstantakos, V., & Laopoulos, T. (2006). Power measuring technique for built-in test purposes. Paper presented at the IEEE instrumentation and measurement technology conference (IMTC), Sorrento, Italy, 24-27 April (pp. 90-95).
- Krintz, C., Wen, Y., & Wolski, R. (2004). Application-level prediction of battery dissipation. Paper presented at the international symposium on low power electronics and design (ISLPED), Newport Beach, CA, 9-11 August (pp. 224-229).
- Laopoulos, T., Neofotistos, P., Kosmatopoulos, C. A., & Nikolaïdis, S. (2003). Measurement of current variations for the estimation of software-related power consumption. *IEEE Transactions on Instrumentation and Measurement*, 52(4), 1206-1212.
- Liu, S., & Sun, D. (2014). Minimizing energy consumption of wheeled mobile robots via optimal motion planning. *IEEE/ASME Transactions on Mechatronics*, 19(2), 401-411.
- Maxim Integrated. (2020). MAX44299 current and voltage sense with power measurement. Retrieved from <https://www.maximintegrated.com/en/products/analog/amplifiers/MAX44299.html>
- Mei, Y., Lu, Y.-H., Hu, Y., & Lee, C. (2004). Determining the fleet size of mobile robots with energy constraints. Paper presented at the IEEE international conference on intelligent robots and systems (IROS), Sendai, Japan, 28 September–2 October (Vol. 2, pp. 1420-1425).
- Mei, Y., Lu, Y.-H., Hu, Y., & Lee, C. (2005). A case study of mobile robot's energy consumption and conservation techniques. Paper presented at the IEEE international conference on advanced robotics (ICAR), Seattle, WA, 18-20 July (pp. 492-497).
- Mei, Y., Lu, Y.-H., Hu, Y., & Lee, C. (2006). Deployment of mobile robots with energy and timing constraints. *IEEE Transactions on Robotics*, 22, 507-522.
- Nakutis, I. (2009). Embedded systems power consumption measurement methods overview. *Measurements*, 44(2), 29-35.
- Narayanan, D. (2005). Software power measurement (Technical Report No. MSR-TR-2005-51). Microsoft. Retrieved from <https://www.microsoft.com/en-us/research/publication/software-power-measurement>
- Nikolaïdis, S., & Laopoulos, T. (2001). Instruction-level power consumption estimation embedded processors low-power applications. Paper presented at the IEEE international workshop on intelligent data acquisition and advanced computing systems: Technology and applications, Crimea, Ukraine, 1-4 July (pp. 139-142).
- Robotis. (2020). Turtlebot3 burger. Retrieved from <https://emanual.robotis.com/docs/en/platform/turtlebot3/overview>
- Tokekar, P., Kamad, N., & Isler, V. (2011). Energy-optimal velocity profiles for car-like robots. Paper presented at the IEEE international conference on robotics and automation (ICRA), Shanghai, China, 9-13 May (pp. 1457-1462).
- Trzynadłowski, A. M. (1988). Energy optimization of a certain class of incremental motion dc drives. *IEEE Transactions on Industrial Electronics*, 35(1), 60-66.
- Wahab, M., Rios-Gutierrez, F., & Shahat, A. E. (2015). Energy modeling of differential drive robots. Paper presented at the IEEE SoutheastCon regional conference, Fort Lauderdale, FL, 9-12 April (pp. 1-6).
- Wang, J. B., Yang, Y. M., & Li, J. (2013). A minimum-energy consumption control algorithm for omnidirectional mobile robots. *Advances in energy science and technology*, 291, 2408-2411.
- Wolf, F., Kruse, J., & Ernst, R. (2002). Timing and power measurement in static software analysis. *Microelectronics Journal*, 33(1-2), 91-100.
- Xiao, X., & Whittaker, W. (2014). Energy considerations for wheeled mobile robots operating on a single battery discharge (Technical Report No. CMU-RI-TR-14-16). CMU-RI-TR-14-16, Carnegie Mellon University Robotics Institute. Retrieved from <https://ri.cmu.edu/pub/files/2014/8/TR-14-16.pdf>
- Zorbas, D., & Razafindraambo, T. (2015). Modeling the power consumption of a wifobot and studying the role of communication cost in operation time (Technical Report No. hal-01357485). Inria Lille - Nord Europe. Retrieved from <https://hal.inria.fr/hal-01357485/document>

## Biographies

**FLAVIO CABRERA** is an assistant professor of electrical engineering at the Pennsylvania State University – Berks Campus. He earned his BS degree in electrical engineering from the Universidad Nacional de Colombia, Bogotá (Colombia) in 1997; his MS degree in electrical engineering from The City College of New York, The City University of New York in 2006; and PhD in electrical engineering from the City University of New York in 2012. Dr. Cabrera's research interests include mobile robotics, multi-robot systems, wireless sensor networks, energy efficiency, and energy scavenging for mobile robotic and small electronic applications. Dr. Cabrera may be reached at [fhc4@psu.edu](mailto:fhc4@psu.edu)

# PLANTAR PRESSURE MONITORING SYSTEM FOR DIABETIC FEET

Sanjeevi Chitikeshi, Old Dominion University; Aaron Isaac Kelman, Plasser American Corporation;  
Shirshak Dhali, Old Dominion University; Ajay Mahajan, University of Akron

## Abstract

Plantar pressure plays a major role in foot problems in diabetic patients. With an increase of pressure in diabetic patients' feet, it creates multiple issues including the interruption of blood flow, which is compounded by a loss of sensory feedback. These issues in conjunction lead to the development of demal ulcerations, necrosis, and, ultimately, partial or total amputation of a patient's foot or possible other appendages. Current non-invasive treatments such as custom-made shoe inserts are not very effective if the patients' feet develop problems in other areas or there are changes in the severity of the problem. In this paper, the authors present a framework for the design of an intelligent shoe insert that monitors foot pressures in diabetic patients to inform them when critical thresholds are exceeded. A prototype design was tested and data were obtained from different subjects of varying heights and weights. The results were consistent with plantar pressures reported by others.

## Introduction

Diabetes is a disease in which the body's ability to produce or respond to insulin is impaired, resulting in abnormal metabolism of carbohydrates and elevated levels of glucose in the blood and urine. This is a disease that affects 30.3 million people in the U.S. alone, as well as there being 1.5 million newly diagnosed patients each year (American Diabetes Association, 2013). As the number of patients increases, so does the cost of treatments and the number of medical personnel needed to tend to these patients. In 2012, \$245 billion dollars was spent domestically on treatments, while in 2017, \$327 billion dollars was spent on treatment (Center for Disease Control and Prevention, 2014). Diabetes is a life threatening, costly, chronic disease. It is estimated that 60%-70% of people afflicted with diabetes have different forms of nerve damage that occurs in the feet or hands. Among these people, approximately 15% will experience foot ulcers or more severe related issues including amputation. In the U.S. each year there are more than 82,000 amputations performed on people afflicted with diabetes.

It is believed that these patients begin to develop foot problems that stem from different issues, two of which are circulatory problems and peripheral neuropathy. Circulatory problems cause foot ulcers, because less blood reaches the foot and deprives it of oxygen. When the foot is deprived of oxygen, the person's foot becomes more vulnerable to injury and slows the foot's ability to heal the injury. Peripheral

neuropathy is nerve damage in the feet or lower legs, and diabetes is the most common cause of this problem. When nerves in the feet become damaged, they are unable to detect pain or discomfort. The cause of this is not known but it is speculated to be the result of an excess of glucose in the bloodstream, and the accumulation of these sugars is thought to form a casing around the nerves (Gabbay, Merola, & Field, 1966). This is one of the main contributions to demal ulcerations, necrosis, and amputations. With Peripheral neuropathy combined with circulatory problems, the shape of the patient's foot will change but the pressure patterns will stay the same (Santos-Longhurst, 2017; American Diabetes Association, 2018).

For healthy people, the pressure patterns in the foot are continuously changing, whereas a diabetic patient's feet are not able to do so. This exposes their feet to very high peak pressures that are located at the same place for long periods of time. Currently, there are only a few ways to treat issues with the foot; these treatments include custom-made shoe inserts, patellar tendon-bearing braces, vitamins, faradic stimulations, rocker bottom soles, surgical fusion non-weight-bearing cast immobilization, and amputations. There are problems with each of these treatments. The issue with custom-made shoe inserts is that they apply pressure relief to certain areas, which is a problem because the area where ulcers can develop is constantly changing and it will eventually move out of the area where the pressure is being relieved (Zangaro & Hull, 1999). Patellar tendon-bearing braces (PTBs) reduce pressure on the hind foot, while not relieving pressure on the mid- or forefoot. There are prescription PTBs but they need to be monitored and adjusted frequently (Saltzman, 1992). Faradic stimulations are when a patient is hooked up to a low-frequency alternating current that is delivered to conductive pads that stimulate the motor points of the muscle in order to trigger muscle contractions.

These stimulations are used to help reduce pain and help condition muscles of the leg and feet; the problem with these stimulations is that they are painful and are not always successful (Pieber, Herceg, & Patemostro-Sluga, 2010). Soles are like custom sole inserts, they reduce pressure on one's foot in concentrated areas. The disadvantage of this method is that as one begins to do physical activity, the foot experiences more pressure than if the person were using regular shoes with no sole (Dubinsky and Miyasaki, 2010; Lin, Su, Chung, Hsia, & Chang, 2017). Lastly, surgical options include amputations and non-weight-bearing casts. A non-weight-bearing cast is a foot-care technique that is used when a patient is in post-surgery. It is used to protect the area that was operated on. Amputations were something that

---

this current study tried to avoid, since getting any appendage amputated drastically changes a patient's life (American Orthopedic Foot & Ankle Society, 2020).

In the area of hemodynamic modeling of the human foot (Gefen, Megido-Ravid, Itzchak, & Arcan, 2000; Jahss, 1991; Gu & Asada, 1999; Vinik & Mehrabyan, 2004), a lumped-parameter model-based simulation that described the dynamics of the human thermoregulatory system was developed. This approach captured the dynamic behavior of the circulation as well as the thermal, and neural control subsystems. The methodology used in these prior studies was used as the basis for the development of the foot model in this current study. The long-term research plan was to develop a piezoelectric embedded sensor on a smart-shoe insert system that would be self-powered and be smarter and more adaptive, when compared to current treatments for this problem (Saltzman, Johnson, Goldstein, & Donnelly, 1992; Dargis, Pantelejeva, Jonushaite, Vileikyte, & Boulton, 1999; Faglia, Favales, Quarantiello, Brambilla, Rampoldi, & Morabito, 1996; Levin, 1995; Armstrong & Lavery, 1996).

The internal foot derangements, neuropathy, and peripheral vascular disease result in diabetic foot ulcers. Neuropathy is the impairment of nerve functions. The cause of neuropathy is not completely known but is speculated to be a result of hyperglycemia, which can lead to dermal ulcerations, necrosis, and, ultimately, to partial or total amputation of the foot (Nelson, Gohdes, Everhart, Hartner, Pettitt, & Knowler, 1988). It is believed that elevated plantar pressure plays a major role in neuropathic foot problems in diabetes patients. The elevated plantar pressure values, plantar tissue stiffness, and skin temperature have been explored in diabetic foot health. One of the causes of the diabetic foot is the development of ulcers at the highest-pressure sites due to plantar tissue stiffening. These effects were studied using MRI scans of the indentation of a sphere into the plantar tissue (Gefen, Megido-Ravid, Azariah, Itzchak, & Arcan, 2001).

In this same study, the measurements of effective shear and elastic module were higher for the diabetic plantar tissue compared with that of non-diabetic feet. Another study (Abouaisha, van Schie, Griffiths, Young, & Boulton, 2001) also found a strong inverse relationship between plantar tissue thickness and dynamic foot pressure measurements. During walking and running, the sole underneath the metatarsal heads acts as a shock absorber. In the study by Hsu, Tsai, Chen, Shau, Chung-Li, Chen, & Chang (2005), the authors found that the main protection against the development of metatarsalgia and foot ulceration was the mechanical properties of the sole. To further evaluate this, mechanical properties such as unloaded thickness, compressibility index, elastic modulus, and energy dissipation ratio of the soles of 20 healthy subjects were measured using ultrasonography (Hsu et al., 2005). The unloaded thickness decreased progressively from the first to the fifth metatarsal heads. Also, using regression analysis, the authors showed

that these properties increased significantly with age and body weight. Another study was done at University of Texas on activity patterns of patients with diabetic foot ulcerations (Armstrong, Lavery, Kimbriel, Nixon, & Boulton 2003). The daily activity steps were measured using a removal cast walker device. The results were a poor healing process when diabetic foot patients did not wear the device. The work from this current study helps in these kinds of processes by monitoring continuous plantar pressure and correlating that to patient activity.

In a study by Lavery et al. (2004), the authors explored the usefulness of at-home, infrared temperature monitoring as a preventative tool in individuals with extremity ulceration and amputation. Temperatures on the sole of the foot were measured two times a day and, in the experiment, it was considered that the elevated temperatures ( $> 4^{\circ}\text{F}$  compared with the opposite foot) resulted in ulceration due to inflammation at the site of measurement. When temperature measurements were high, the subjects were asked to reduce their activity and contact the study nurse. This study, however, did not take plantar pressure values into consideration. This current study, the authors included temperature monitoring to enhance the healing process of foot ulcerations in diabetic feet. In a study by Collier and Brodbeck (1993), the authors explored the relationship between the loss of protective pressure sensation in the foot and the formation of plantar calluses. Semmes-Weinstein monofilaments were used to monitor the pressure-sensing quality. From that study, the authors suggested that not only pressure sensation but also other factors such as changes in the foot due to age and proper footwear should be included in the assessment of foot health and the prevention of foot ulcerations. This current study built on the foundation for plantar pressure data measurement and data gathering and included subjects of different ages and weights. From the study, the authors concluded that there is no clear answer of mathematical equation-type relationship between plantar pressure and diabetic foot health, but other factors should be included, such as temperature and blood flow.

## Design and Implementation

This design approach in this current study was a continuation of work done by Chitikeshi, Chitikeshi, Gupta, Mahajan, and Schoen (2006). In that previous work, the authors did not include filters and data were collected only on laboratory weight. In that previous work, data were not analyzed extensively in terms of regression analysis and verification of the importance of pressure sensor location on the insole of the shoe. This aspect was accounted for in this current work. The proposed pressure monitoring system would allow doctors and engineers to monitor how much pressure a patient's foot is experiencing and where the affected areas are located. It is important to monitor the pressure in diabetic feet, since most of their health issues come from the feet. With an increased amount of pressure, the chance for ulcers to develop also increases. Along with the development of

ulcers, the circulation in the patients' feet is also highly reduced. The proposed system would monitor the pressure that diabetic patients put on their feet, using a sensor array placed on a shoe insole. The output voltage of the sensor is then be amplified by an active filter. Once amplified, a microcontroller and data transmitter (RS-MAX 232) are integrated such that users are able to see the different pressure values on a computer. These voltage values correspond to different weight values gathered through testing. The overall system included a microcontroller, computer, four pressure sensors on a shoe insole, power supply, oscilloscope, a function generator, and an operational amplifier circuit. In laboratory environment testing, an external DC power source was used to power up the system.

In this current paper, the authors discuss the design and implementation of a plantar pressure monitoring system when a variety of different weights and pressures are exerted. The scope of this project was to implement a sensor array in a shoe insole, with signal processing utilizing active filters. The weight monitoring system was based on a microcontroller embedded system. Data were gathered and testing occurred at every step of the project, including during simulation and the implementation phase. The objective of this project was to create a system that would be able to accurately measure pressure sensor data placed on a shoe insole and establish a correlation between the weight and height of a person from the measured pressure data. The system was implemented to allow for future expansion. The sensor array and placement in relation to the patients' foot was critical. In this study, four sensors were placed on a custom shoe insole so that each sensor gave an accurate reading. The sensor signals were filtered and amplified before being fed into a microcontroller for analysis.

## Pressure Sensor and Sensing Array

With the wide variety of sensors that were available, the authors selected the FlexiForce sensor. These sensors act similarly to a variable resistor. When there are no forces acting on the resistor, it has a high resistance, on the order of  $M\Omega$ . When maximum force is applied, the resistance is a few  $k\Omega$ . Since weight and resistance have an inverse relationship, that means that the higher the weight on the sensor the higher the output voltage. First, it was important that the sensing area be a circle as opposed to a square, because a circle is a more concentrated area, whereas a square is more likely to have more variations across the entire surface. Second, during most of the year, the interior of a shoe generates a lot of heat, so it was important that the sensor be able to withstand high heat. The third desirable quality was that it would be able to handle a large force range of 0-445N (or 100 lb.) for each sensor. The FlexiForce ESS301 pressure sensor was chosen in order to meet these criteria. The ESS301 sensor is a connector with two male pins, a  $9.53 \text{ mm}^2$  sensing area, and a thickness of 0.203 mm. The authors felt that a thicker sensor could cause the system to be uncomfortable for the person to use.

Of the two pins, one was for the reference voltage and the other was the output pin. There were two recommended reference voltage options: AC and DC. The AC option was a  $5V_{\text{peak-to-peak}}$  square wave with a 50% duty cycle. The DC option offered any voltage between 0.25V and 1.25V. For this system, AC voltage was used.

## Filter and Amplification System

The design of this foot pressure monitoring system required the use of a filtering system to filter out noise from the signals. There was a choice to be made between three different filters. The options were either a low-pass, high-pass, or band-pass filter. While walking, the human foot moves a fair amount but does not experience a lot of rapid or dramatic changes. Thus, a low-pass filter was chosen. Still, both band-pass and low-pass filters were tested. Once the noise had been filtered out, the next step was to amplify the voltage output of the sensor to interface with the microcontroller. The circuit of Figure 1 shows the amplifier for which the relationship between the sensor and the feedback resistor determines the gain of the system. In a system such as this, if the resistance of the feedback resistor were to increase, the system would become much more sensitive to weight.

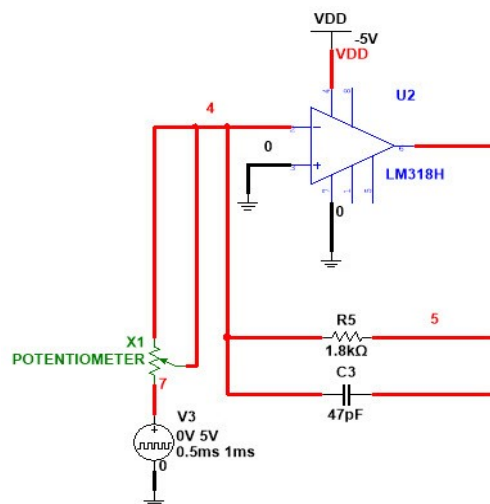


Figure 1. Basic amplification circuit and feedback resistance variations.

The same circuit with a low-pass filter circuit was used to calibrate the pressure sensor. However, the gain was insufficient so the raw signals had to be filtered. Several active filter options were investigated. First, an active band-pass filter was designed to evaluate the results and sensitivity of the sensors. The advantage of a band-pass filter is its narrow bandwidth, which would reduce noise. Since the foot is close to a static object, a lower cutoff frequency of 30 Hz and an upper cutoff frequency of 150 Hz were chosen. These frequency values were chosen based on a normal person's foot speed within a range of about 100Hz. The resis-

tors were chosen to be 10 KΩ. Once the upper cutoff, lower cutoff, and center frequencies were determined, the two capacitance values were obtained from Equations 1 and 2:

$$F_L = \frac{1}{2\pi RC_1} \quad (1)$$

where,  
 $F_L = 30 \text{ Hz}$   
 $R = 10 \text{ K}\Omega$   
 $C_1 = 530.5 \mu\text{F}$

$$F_H = \frac{1}{2\pi RC_2} \quad (2)$$

where,  
 $F_H = 150 \text{ Hz}$   
 $R = 10 \text{ K}\Omega$   
 $C_2 = 106.1 \text{ nF}$

The response of this band-pass filter was not stable for very low frequencies coming off of the pressure sensors, due to very low foot speeds. To overcome this problem, a second-order low-pass filter was designed. A second-order filter was chosen so that a steeper frequency response could be achieved. In this filter, a response rate of twenty was still used, but the cutoff frequency was changed to one 100 Hz and a set capacitor of 2.2 μF was selected. All the capacitors and amplifier resistor component values were determined using Equations 3 and 4:

$$F_C = \frac{1}{2\pi RC} \quad (3)$$

$$C = \frac{1}{2\pi RF_C} \quad (4)$$

where,  
 $F_C = 100 \text{ Hz}$   
 $C = 2.2 \mu\text{F}$   
 $R = 724\Omega$

To maintain stability, the gain had to be a maximum of three. The Quality factor value was chosen as 20. Using these values, the non-inverting amplifier gain resistor values were computed using Equations 5 and 6:

$$A = 3 - \frac{1}{Q} \quad (5)$$

where,  
 $Q = 20$   
 $A = 3 - \frac{1}{20} = 2.95$

And the non-inverting amplifier resistors were:

$$A = 1 + \frac{R_f}{R_i} \quad (6)$$

Since  $R_f$  was determined to be 724Ω, that yielded an  $R_i$  value ≈ 371Ω.

The resistor values were adjusted to standard resistor values, which changed the cutoff frequency to 107 Hz. Figure 2 shows the final circuit (developed in *Multisim*). After comparing second-order and first-order low-pass filters, no significant improvements were noted in the second-order filter. Hence, in order to reduce the number of components, a first-order filter was chosen for the final design circuit.

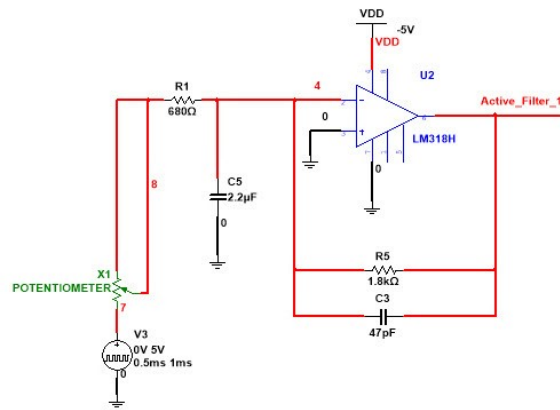


Figure 2. Filter circuit.

## Microcontroller and Computer Interface

Figures 3 and 4 shows the PIC18F4550 microcontroller that was chosen for reading the data from the active filters. This microcontroller has a built-in low-frequency ADC converter, RS-232 communication port to transmit the data to PC, and sufficient digital I/O pins to interface to the LCD display and other alerting devices that could be included in the system.

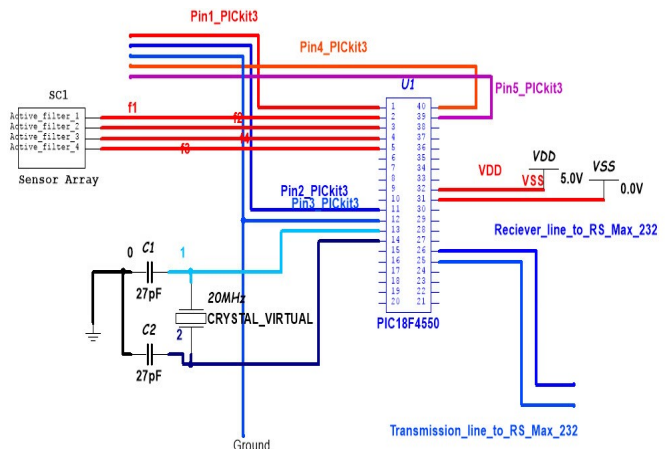


Figure 3. Microcontroller interfacing circuit.

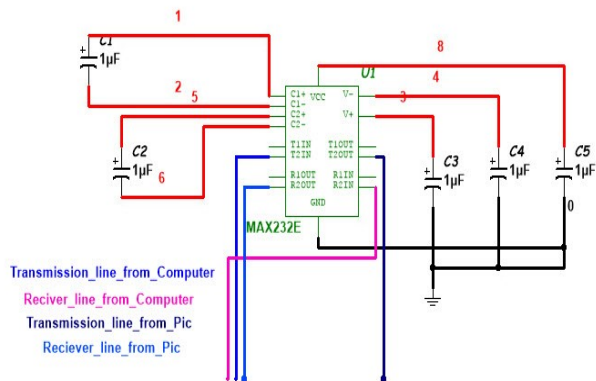


Figure 4. Data transmission to the PC using the MAX 232 circuit.

## Results and Discussion

The first step before starting the testing phase was to choose the sensor locations. The first sensor was located underneath the big toe; this location was chosen because putting a sensor there would help determine if the person were performing a heel-to-toe or toe-to-heel movement. The second sensor was located at the sole of the foot; this location is incredibly important because it is a very common location for ulcers to develop. The third sensor was located at the heel; this location was chosen since this is where most of the pressure in the foot exists. Lastly, the fourth sensor was located at the arch of the foot in order to gain a stable reading from individuals with flat feet.

Before collecting the data from the four sensors, it was very important to calibrate the sensors using known weight/force values. The calibration step was done using a compression machine, which outputs an exact amount of force on an object. Figure 5 shows how a pressure sensor was attached to the compression machine and a known force was applied to the sensor. Amplified and filtered output voltages were recorded for a range of weights and forces.

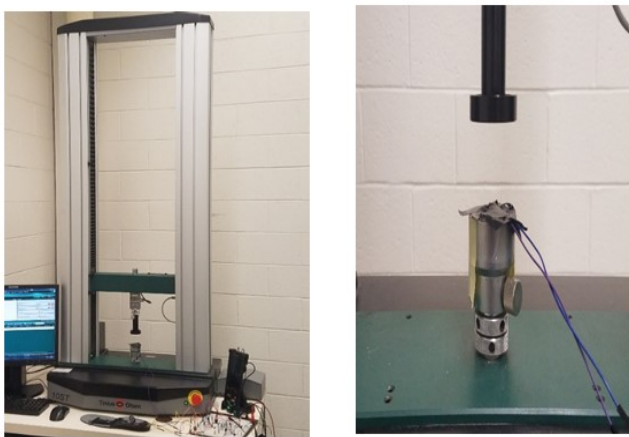


Figure 5. Data collection using a compression machine.

Figure 6 shows a graph of data obtained from the compression machine on one sensor. The graph shows that as pressure goes up so does the output voltage of the system, but it is nonlinear and starts to saturate at higher forces.

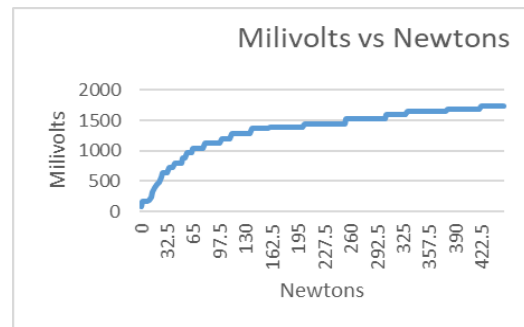


Figure 6. Sensor output voltage for known forces.

The next step in the testing phase was to use the aforementioned calibration results and collect data from the sensors placed on the shoe insole onto which force was applied from human feet. Pressure data were gathered to better understand sensor response and placement of the sensors. A total of thirty subjects were tested and their responses to the four sensors on each foot were recorded. The foot conditions of these student subjects were not known. However, given their young age, it was assumed that these students likely did not have diabetic feet. For each subject, a set of three data readings was obtained. Figure 7 shows a sample compilation of the sensor voltage data versus the weight of the subject. The students are listed in increasing weight with “Student 1” in the middle with an ideal body mass index (BMI). Based on these data, there were certain notable trends for these subjects, when those of lower weights were compared to those of higher weights. The volunteers that were closer to an ideal body weight for their frame tended to have much higher peaks in pressure.

For example, “Student 1” in Figure 8 was very close to ideal body weight. This subject had much higher peaks in the forefoot as well as the heel but had very low pressure in the other two locations, as would be expected for a normal foot. Normally, there are three main points of highest load on the sole of the feet: the central part of the heel and the 1<sup>st</sup> and 4<sup>th</sup>/5<sup>th</sup> metatarsal heads (Sutkowska, Sukowski, Sokolowski, Frank, & Dragon, 2019). Specific sensor voltage showed a wide variation with weight and no trend-line (Figure 8 shows sensors 1 and 2 of the right foot). However, the average of the four right foot sensors shows a linear increase with the subject’s weight, as expected. The data suggest that the weight distribution of the body on the planter differs from person to person. This result is consistent with published data by Sutkowska et al. (2019) on distribution of the highest planter pressure region in patients with diabetes. The authors concluded that it is the deviation from the normal distribution that is indicative of a diabetic foot. Furthermore, they suggest that knowing the absolute pressure is not as critical as the planter pressure distribution.

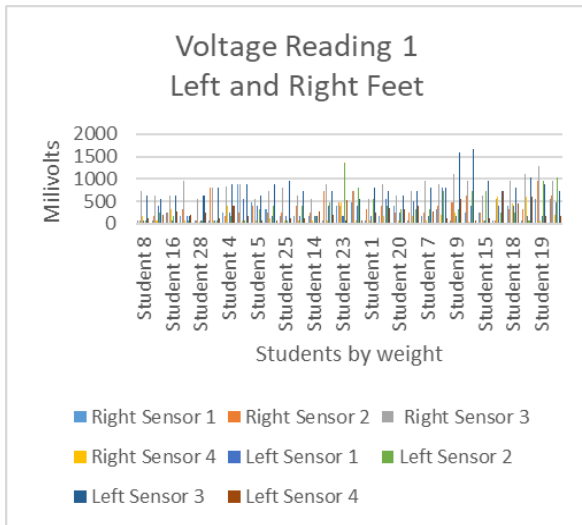


Figure 7. Subject data (organized by weight).

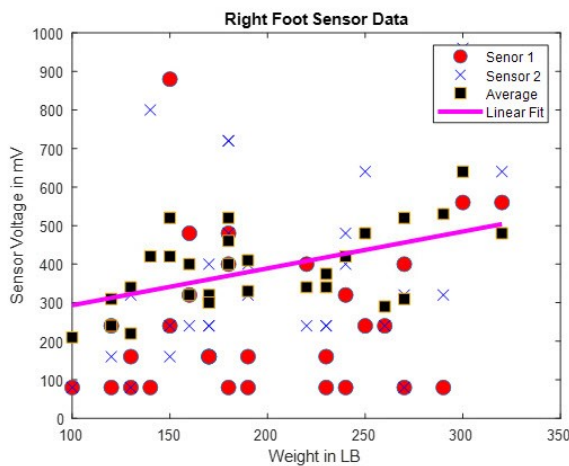


Figure 8. Right-foot sensor data regression with subjects' weight.

## Conclusions and Future Work

A framework for the design and implementation of a plantar pressure monitoring system was presented. A simple, cost-effective architecture using a microcontroller was tested to collect and analyze foot pressure. In this paper, the authors also discussed tradeoffs in processing of the noisy signal and the choice of sensors. The designed system was calibrated using a compression machine followed by the collection of data for thirty subjects of varying height and weight. The analysis of the data for the thirty-student sample showed peaks at the normal physiological locations, as expected. These results signify the importance of plantar pressure underneath the foot of a diabetic patient. Future work should include the use of this designed system along with other sensors and more mathematical models for monitoring the health of the diabetic foot.

## Acknowledgments

This work was supported in part by Old Dominion University - Summer 2017 Faculty Research Fellowship Award. The authors would like to thank the ODU Office of Research for providing this financial support to successfully complete this work and get preliminary data from the developed system.

## References

Abouaeha, F., van Schie, C. H., Griffiths, G. D., Young, R. J., & Boulton, A. J. (2001). Plantar tissue thickness is related to peak plantar pressure in the high-risk diabetic foot. *Diabetic Care*, 24(7), 1270-1274. doi: 10.2337/diaca.24.7.1270.

American Diabetes Association. (2013). *Common Terms*. Retrieved from [www.diabetes.org/diabetes-basics/common-terms/?loc=mp-slabnav](http://www.diabetes.org/diabetes-basics/common-terms/?loc=mp-slabnav)

American Diabetes Association. (2018, March 22). *Statistics About Diabetes*. Retrieved from <http://www.diabetes.org/diabetes-basics/statistics>

American Orthopedic Foot and Ankle Society. (2020). *How to Be Non-Weightbearing After Surgery*. Retrieved from [www.aofas.org/footcaremd/how-to/foot-injury/Pages/How-to-Be-Non-weightbearing-After-Surgery.aspx](http://www.aofas.org/footcaremd/how-to/foot-injury/Pages/How-to-Be-Non-weightbearing-After-Surgery.aspx)

Armstrong, D. G., Lavery, L. A., Kimbriel, H. R., Nixon, B. P., & Boulton, A. J. M. (2003). Activity patterns of patients with diabetic foot ulceration: patients with active ulceration may not adhere to a standard pressure off-loading regimen. *Diabetes Care*, 26(9), 2595-7. doi: 10.2337/diaca.26.9.2595.

Armstrong, D. G., & Lavery, L. A. (1996). Is prophylactic diabetic foot surgery dangerous? *Journal of Foot Ankle Surgery*, 35, 585-89.

Center for Disease Control and Prevention. (2014, June 17). *Diabetes Latest*. Retrieved from [www.cdc.gov/features/diabetesfactsheet/](http://www.cdc.gov/features/diabetesfactsheet/)

Chitikeshi, V., Chitikeshi, S., Gupta, R., Mahajan, A., & Schoen, M. (2006). *An Intelligent foot monitoring system for diabetic patients to prevent foot ulcers*. Paper presented at the ASME International Mechanical Engineering Congress and Exposition Conference, Chicago, IL, November 5-7.

Collier, J. H., & Brodbeck, C. A. (1993). Assessing the diabetic foot: Plantar callus and pressure sensation. *Diabetes Educ.*, 19(6), 503-8. doi: 10.1177/014572179301900605.

Dargis V., Pantelejeva, O., Jonushaite, A., Vileikyte, L., & Boulton, A. J. (1999). Benefits of a multidisciplinary approach in the management of recurrent diabetic foot ulceration in Lithuania: a prospective study. *Diabetes Care*, 22(9), 1428-1431.

Dubinsky, R. M., & Miyasaki J. (2010). Efficacy of transcutaneous electric nerve stimulation in the treatment of pain in neurologic disorders (an evidence-based review). *Neurology*, 74(2), 173-176. doi: 10.1212/WNL.0b013e3181c918fc.

- Faglia, E., Favales, F., Quarantiello, A., Brambilla, G., Rampoldi, A., & Morabito, A. (1996). Feasibility and effectiveness of Peripheral percutaneous transluminal balloon angioplasty in diabetic subjects with foot ulcers. *Diabetes Care*, *19*(11), 1261-1264.
- Gabbay, K. H., Merola, L. O., & Field, R. A. (1966). Sorbitol pathway: presence in nerve and cord with substrate accumulation in diabetes. *Science*, *151*(3707), 209-10. doi: 10.1126/science.151.3707.209.
- Gefen, A., Megido-Ravid, M., Itzhak, Y., & Arcan, M. (2000). Biomechanical Analysis of the Three-Dimensional Foot Structure During Gait: A Basic Tool for Clinical Applications. *Journal of Biomechanical Engineering*, *122*, 630-639.
- Gefen, A., Megido-Ravid, M., Azariah, M., Itzhak, Y., & Arcan, M. (2001). Integration of plantar soft tissue stiffness measurements in routine MRI of the diabetic foot. *Clinical Biomechanics*, *16*(10), 921-925. DOI: [https://doi.org/10.1016/S0268-0033\(01\)00074-2](https://doi.org/10.1016/S0268-0033(01)00074-2)
- Gu, B., & Asada, H. (1999). Multi domain co-simulation of the human thermoregulatory System. *Proceedings of the ASME: Dynamic Systems and Control Division*, Vol. 67, (pp. 553-559).
- Hsu, C., Tsai, W., Chen, C. P., Shau, Y., Chung-Li, W., Chen, M. J., & Chang, K. (2005). Effects of aging on the plantar soft tissue properties under the metatarsal heads at different impact velocities. *Ultrasound in Medicine & Biology*, *31*(10), 1423-1429.
- Jahss, M. H. (1991). Disorders of the foot and ankle: Medical and surgical management. (2nd ed.). W.B. Saunders, Philadelphia.
- Lavery, L. A., Higgins, K. R., Lanctot, D. R., Constantinides, G. P., Zamorano, R. G., Armstrong, D. G. ... Agrawal, C. M. (2004). Home monitoring of foot skin temperature to prevent ulceration. *Diabetes Care*, *27* (11), 2642-7. doi: 10.2337/diacare.27.11.2642.
- Levin, M. E. (1995). Preventing amputations in the patient with diabetes. *Diabetes Care*, *18*(13), 83-92.
- Lin, S-Y., Su, P-F., Chung, C-H., Hsia, C-C., & Chang, C-H. (2017). Stiffness Effects in Rocker-Soled Shoes: Biomechanical Implications. *PLoS One*, *12*(1), e0169151 doi: 10.1371/journal.pone.0169151
- Nelson, R. G., Gohdes, D. M., Everhart, J. E., Hartner, J. A., Pettitt, D. J., & Knowler, W. C. (1988). Lower extremity amputations in NIDDM: 12-yr follow-up study in Pima Indians. *Diabetes Care*, *11*(1), 8-16. doi: 10.2337/diacare.11.1.8.
- Pieber, K., Herceg, M., & Patemostro-Sluga, T. (2010). Electrotherapy for the treatment of painful diabetic peripheral neuropathy: a review. *Journal of Rehabilitation Medicine*, *42*(4), 289-295. doi: 10.2340/16501977-0554.
- Saltzman, C. L., Johnson, K. A., Goldstein, R. H., & Donnelly, R. E. (1992, Jan). The patellar tendon-bearing brace as treatment for neurotrophic arthropathy: A dynamic force monitoring study. *Foot & Ankle*, *13*(1), 14-21.
- Saltzman, L. (1992). The Patellar Tendon-Bearing Brace as Treatment for Neurotrophic Arthropathy: a Dynamic Force Monitoring Study. *Foot & Ankle*, U.S. National Library of Medicine. Retrieved from [www.ncbi.nlm.nih.gov/pubmed/1577336](http://www.ncbi.nlm.nih.gov/pubmed/1577336)
- Santos-Longhurst, A. (2017). *Type 2 Diabetes Statistics and Facts*. Healthline Media. Retrieved from [www.healthline.com/health/type-2-diabetes/statistics#2](http://www.healthline.com/health/type-2-diabetes/statistics#2)
- Sutkowska, E., Sukowski, K., Sokolowski, M., Frank, E., & Dragon, S. (2019). Distribution of the highest plantar pressure regions in patients with diabetes and its association with peripheral neuropathy. *Journal of Diabetic Research*, ID 7395767. Retrieved from <https://doi.org/10.1155/2019/7495767>
- Vinik, A. I., & Mehrabyan, A. (2004). Diabetic neuropathies. *Medical Clinics of North America*, *88*(4), 947-999.
- Zangaro, G. A., & Hull, M. M. (1999). Diabetic neuropathy: Pathophysiology and prevention of foot ulcers. *Clinical Nurse Specialist*, *13*(2), 57-65. <https://doi.org/10.1097/00002800-199903000-0000>

## Biographies

**SANJEEVI CHITIKESHI** is an assistant professor in the Electrical Engineering Technology Program at Old Dominion University. He earned his PhD in electrical engineering in 2008 from Southern Illinois University. Dr. Chitikeshi's research interests include biomedical, mechatronics, controls, robotics, embedded systems, curriculum development, and big data. Dr. Chitikeshi may be reached at [schitike@odu.edu](mailto:schitike@odu.edu)

**AARON ISAAC KELMAN** is an electrical design engineer at Plasser American Corporation. He earned his BS degree in electrical engineering technology in 2018 from Old Dominion University. Mr. Kelman may be reached at [akelm001@odu.edu](mailto:akelm001@odu.edu)

**SHIRSHAK DHALI** is a professor in the Electrical and Computer Engineering Department at Old Dominion University. He also served as ECE Department Chair and Associate Dean for Research in the College of Engineering at ODU. Dr. Dhali's research interests include electronics, plasma, biomedical, mechatronics and controls. Dr. Dhali may be reached at [sdhali@odu.edu](mailto:sdhali@odu.edu)

**AJAY MAHAJAN** is a professor of mechanical engineering/biomedical engineering at the University of Akron. He joined UA in 2009 as the Associate Dean for Research for the College of Engineering. He also served as Special Assistant to the President for Innovation and the Associate Vice President for Innovation before returning to a full-time faculty position within the Mechanical Engineering and Biomedical Engineering departments. Dr. Mahajan's research interests include intelligent systems, robotics, controls, biomedical devices, data analytics, and smart genomics. Dr. Mahajan may be reached at [majay@uakron.edu](mailto:majay@uakron.edu)

# ENERGY CONSUMPTION IN EXTRUSION-BASED METAL ADDITIVE MANUFACTURING

Mehmet Emre Bahadir, Southeastern Louisiana University; Caleb Lagarrigue, PSX Worldwide Audiovisual Technologies; Juan Gonzalez, Pike Electric

## Abstract

Human activities are harming our planet through global warming, environmental pollution, and natural resource depletion. There is an urgent need to improve the environmental performance of those activities. Manufacturing and related activities are recognized as the most harmful human activities, in terms of their impact on the environment. The first step in improving environmental performance is measuring and analyzing the current environmental effects of manufacturing activities. In this context, additive manufacturing (AM), also known as 3D printing, has become one of the mainstream manufacturing methods, and its environmental analysis is becoming necessary. Previous studies have reported the environmental footprint of 3D printing technologies, mainly for laser and electron beam sintering processes. In this current study, the authors concentrated on an energy consumption analysis of a novel AM technology known as bound metal deposition (BMD), which is capable of 3D printing of metal parts and assemblies through a three-step process: printing, debinding, and sintering. The effects of three printing parameters (part orientation, layer thickness, and print pattern) and shape characteristics on the energy consumption were analyzed. A 2<sup>3</sup> factorial experimental design was conducted at two levels for each printing parameter. Energy consumption was recorded during the printing, debinding, and sintering processes. Significant process parameters were identified and possible strategies for reducing energy consumption were discussed.

## Introduction

Human activities are damaging the balance of the ecosystem through the depletion of natural resources and emitting harmful byproducts such as waste and toxic contaminants into the air, water, and soil. In the U.S., industrial activities have been responsible for 23% of greenhouse gas emissions, and electricity generation has been responsible for 25% of greenhouse gas emissions in 2019. In the same year, 2581 billion kWh of electricity was generated at utility-scale electricity generation facilities from fossil fuels, such as coal, natural gas, petroleum, and other gases (U.S. EIA, 2019). Energy consumption analysis of manufacturing systems is a critical area of research in order to understand the current level of energy requirements and to develop methods for reducing energy consumption. Dahmus and Gutowski's work (2004), mainly on machining operations, was one of the earliest studies on the environmental analysis of manufacturing processes. Milling, turning, and drilling processes were researched by Dahmus and Gutowski (2004),

Kara and Li (2011), and He, Liu, Wu, Zhong, & Peng (2012). Recent advances, especially in the speed, precision, and cost of metal additive manufacturing, have placed 3D printing technology as a viable alternative to traditional manufacturing technologies. As these systems start to prevail in certain manufacturing sectors, their environmental evaluation has become a necessity.

One of the first studies conducted on the energy consumption of AM technologies dates back to 1999 (Luo, Ji, Leu, & Caudill, 1999). Later studies have focused on the measurement and analysis of power usage for AM technologies from various perspectives, such as the type of the AM technology, scope (unit process vs. life-cycle), printing parameter (layer height, print pattern, part orientation, shape complexity, etc.), the measure of energy (specific energy consumption, total energy consumption, and energy density), and level of detail (whole system vs. subsystems and whole process vs. stages of the process). The most commonly reported AM technologies are SLS (Luo et al., 1999; Kellens, Dewulf, Deprez, Yasa, & Duflou, 2010; Sreenivasan, & Bourell, 2009; Baumers, Tuck, Wildman, Ashcroft, & Hague, 2011; Baumers, Tuck, Bourell, Sreenivasan, & Hague, 2011; Kellens, Yasa, Renaldi, Dewulf, Kruth, & Duflou, 2011), FDM (Luo et al., 1999; Baumers et al., 2011; Junk & Côté, 2012), SLM (Baumers, Tuck, Hague, Ashcroft, & Wildman, 2010; Kellens, Yasa, Dewulf, & Duflou, 2010; Baumers et al., 2011), EBM (Baumers et al., 2010; Baumers et al., 2011), and DED (Morrow, Qi, Kim, Mazumder, & Skerlos, 2007; Wilson, Piya, Shin, Zhao, & Ramani, 2014; Baumers et al., 2011; Jackson, Van Asten, Morrow, Min, & Pfeffeckorn, 2016).

Kellens et al. (2010) identified eight subsystems of a selective laser melting (SLM) system (laser unit, powder dosage chamber, building platform, coater, XY positioning of the scanner, nitrogen circulation unit, cabinet cooling, and the computer unit) that were responsible for significant energy consumption and collected simultaneous measurements from those subsystems. They noted that with 2.24 kW power usage, the laser unit alone was responsible for 68% of the total power usage of the printing system. In the same study, twelve subsystems were identified for a polymer selective laser sintering (SLS) system (machine tool, process chamber heating, frame heating, platform heating, laser unit, PC, laser cooling, scanners, servos, lightning, cabinet cooling, and lens heating). For the SLS system, the highest energy-consuming units were the laser cooling unit and process chamber heaters with 3 kW and 0.8 kW power, respectively. Yoon et al. (2014) analyzed the energy consumption according to the printing stages. They defined "total energy" as the

total of three distinct steps: initial heating (without printing), heating (during printing), and stage (all other energy consumed).

Specific energy consumption (SEC) is a widely used measure of energy performance that represents the amount of energy usage for a unit mass of material (kWh/kg). SEC is a significant measure, especially for comparative analysis. Yoon et al. (2014) estimated that the SEC of 3D printing processes is 100 times more than the SEC of bulk-deformation processes. Kellens et al. (2010) calculated the specific energy consumption of a polymer SLS system to be between 26.3 and 36.5 kWh/kg, depending on the material type and particle size. Morrow et al. (2007) reported an SEC of 7708 MJ/kg for a DED process with H13 tool steel in a comparative study between milling and additive manufacturing. Baumers et al. (2011) studied DED technology for fabricating 17-4 PH parts and showed that the SEC of the DED system ranged between 241 and 339 MJ/kg.

Another measure used in the literature was energy density. Liu, Li, Fang, and Guo (2018) defined energy density as a “function of energy beam power, scanning speed, beam diameter, layer thickness, and hatch spacing.” Bourell, Co-holich, Chalancon, and Bhat (2017) used energy density as a measure of energy consumption to predict material characteristics. Current studies on energy consumption of metal 3D printing systems have focused on selective laser melting (Baumers et al., 2011; Sachs, Cima, & Cornie, 1990; Baumers et al., 2010; Kellens, Mertens, Paraskevas, Dewulf, & Duflou, 2017; Faludi, Baumers, Maskery, & Hague, 2017), electron beam melting (Baumers et al., 2010; Faludi et al., 2017; Paris, Mokhtarian, Coatanéa, Museau, & Ituarte, 2016), and directed energy deposition additive manufacturing technologies (Morrow et al., 2007; Wilson et al., 2014; Baumers et al., 2011; Jackson et al., 2016).

In Selective laser melting (SLM) and electron beam melting (EBM), a layer of metal powder is sprayed onto the build platform. A laser or electron beam is applied to that layer to melt and fuse the metal particles in a sealed chamber. Directed energy deposition technology uses a laser or electron beam focused on a stream of powder material. The print is created at the melt pool where the energy and material meet. In this current study, the complete fabrication cycle was divided into stages; total energy and the energy for each stage were calculated separately.

## Overview of BMD Technology

Extrusion-based metal additive manufacturing is a relatively new metal 3D printing method that was commercialized in 2018. The method was first introduced by two U.S.-based companies—Desktop Metal and Markforged. Markforged patented its system under the name “Atomic Diffusion Additive Manufacturing” (ADAM), and Desktop Metal uses the term “Bound Metal Deposition” (BMD).

The technology is similar to fused deposition modeling (FDM) 3D printing technology, where a melted material is extruded layer by layer. However, in extrusion-based metal additive manufacturing technology, the material is a mixture of metal powder and a polymer binder, which is commonly used in metal injection molding (MIM) systems. The material mix for the ADAM technology comes in a filament form, while the BDM system uses cylindrical rods. Each rod is 21 grams and there are 200 rods in a material cartridge. Figure 1 shows the rods that are used for the Desktop Metal Studio 3D printer.



Figure 1. 3D printing material for Desktop Metal Studio 3D printers.

The BMD manufacturing process consists of three major steps—3D printing, debinding, and sintering. For each step, there is a dedicated unit. In the 3D printing step, the material mix is heated in the extrusion head to 175°C. At this temperature, the primary binder in the material mix melts and the material is extruded onto a heated build plate layer by layer. During a complete printing job, a raft is first printed in order to provide a level surface and to support the part during the debinding and sintering steps. Next, an interface material, a mixture of ceramic powder and binder, is printed as a thin layer on the raft in order to prevent bonding. Interface material is printed by a separate extruder head. If necessary, to support the part features such as overhangs and bridges, the 3D printer prints support structures underneath those features. As the part is being printed, interface material is applied between the actual part and the support structures. Figure 2 shows a finished 3D-printed part with a raft, interface layer, and actual part. After the printing is finished, the part is held on the build plate until it cools to room temperature. When the part reaches room temperature, it is ready to be removed from the build plate. At this stage, the part is still fragile and is considered a “green” part.

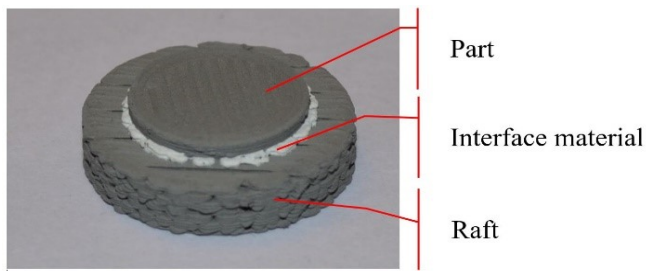


Figure 2. Printed “green” part.

The next step is the debinding step, where the green part is placed into the debinder filled with a debinding solution to dissolve and remove the primary binding material. The exact formula of the feedstock material is proprietary, and Desktop Metal is not sharing with the public; however, typical MIM feedstock consists of 60% metal and 40% binder volumetrically. This ratio is consistent with the fact that the final finished part is 20% smaller volumetrically than the green part. Wax functions as the primary binder in the binder mixture, and plastic acts as the secondary binder. In the debinding chamber, the debinding solution is heated, and most of the primary binder is removed chemically. The remaining plastic binder holds the shape and keeps the part intact. After the chemical debinding phase is completed, the part is called the “brown” part. In the third step, the brown part is placed into a sealed sintering furnace. First, the part is heated slowly to remove the remaining primary and secondary binders in the furnace. When the debinding process is completed, the temperature is raised almost to the melting point in order to fuse the remaining metal particles. The densification process creates solid parts with 96% to 99.8% relative density.

## Method

Energy consumption of the BMD system is analyzed for printing, debinding, and sintering steps separately. Each step is broken down into distinct stages as well. For each step, significant parameters are identified, and their effects on energy consumption are measured. For the 3D printing and debinding steps, experimental runs with different parameters are tested. Measurements are performed using Fluke 1734 three-phase power measurement logger. In the next section, each fabrication step, measurement procedure, and significant parameters are explained. Before the physical production of the part, a 3D virtual model of the part is created. Next, the 3D virtual model is converted into a part file that is compatible with the Desktop Metal 3D printer. For this purpose, Desktop Metal Studio System uses its cloud-based software named Fabricate. The Fabricate software enables users to define parameters for 3D printing, debinding, and sintering operations. After the preparation of the virtual model, the remaining printing steps are very similar to FDM of plastic parts. Next, the model file is uploaded to the 3D printer. The rest of the processes are fully automated.

Before each printing job, the 3D printer calibrates the temperature and location sensors, positions the extruders, raises the print bed, cleans the tips of the nozzles, and heats both extruder heads and the print bed. Initially, the extruder heads are heated to 175°C and the print bed is heated to 65°C. During the printing step, the active extruder head is kept at 175°C, while the idle extruder head is allowed to cool down to 100°C. The temperature of the print bed is always kept at 65°C. The initiation process takes approximately ten minutes. When the 3D printer calibration is completed, the part is printed layer-by-layer on the build plate, starting with a raft. The purpose of the raft is to ensure the adhesion of the part to the build plate and support the part during the debinding and sintering steps. The actual part is printed on the raft by the same extruder head using the same material (metal binder mix).

However, different from the FDM systems, the BMD system deposits a layer of ceramic material between the actual part and the raft in order to prevent fusion of the two. The ceramic material is extruded from the second print head. Every time the 3D printer switches between printing the metal and ceramic material, the printing process pauses to get the next extruder head ready by cleaning, reheating, calibrating, and positioning it. The switch is completed in one and a half minutes. Another process that requires the printer to pause is material auto loading. The print materials are shaped as twenty-one grams of cylindrical rods. The printing process pauses when an extruder head runs out of material and the rods are auto loaded from the material cartridge. The auto loading sequence takes one and a half minutes, too.

For the 3D printing operation, numerous parameters can be adjusted in order to change the print quality, printing time, material consumption, and energy usage. Some of the parameters that can be defined through the Fabricate software are print profile, infill density, layer height, wall thickness, print pattern, print speed, cooling fan speed, support overhang angle, support distance, raft margin, and number of raft layers. Among these parameters, the layer thickness of the print, the orientation of the part on the build plate, and the percentage of infill material are known to significantly affect energy consumption during the 3D printing of FDM parts (Griffiths, Howarth, De Almeida-Rowbotham, Rees, & Kerton, 2016). For this current study, layer height, part orientation, and print pattern were selected to investigate their effects on energy consumption. These three parameters were analyzed at two levels with a 2<sup>3</sup> factorial experimental design. Figure 3 shows the printed test parts—5x10x20 mm rectangular blocks. The size of the rectangular blocks was selected to be small enough to complete the printing processes in a reasonable amount of time. The capacity of the 3D printer was 3 kg for a single part and 6.5 kg for multiple parts. The single-part capacity limit was determined by the maximum load capacity of the sintering furnace.

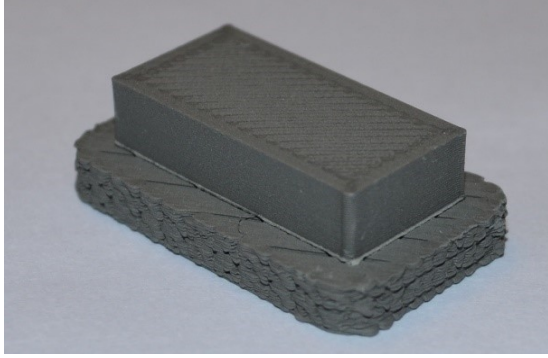


Figure 3. A 3D-printed 5x10x20 mm test piece.

## Layer Height

For the BMD system, layer height is a printing parameter that can be controlled to achieve desired product qualities. Figure 4 shows that the layer height is the thickness of each layer controlled by the movement of the printing platform between layers. When higher values are used, printing time shortens and print resolution decreases. With lower layer height, higher resolution is achieved but energy consumption increases with the total print time. The Desktop Metal Studio 3D printers' layer height can be a minimum of 0.1 mm and a maximum of 0.3 mm, with a recommended height of 0.15 mm. In this current study, experimental parts were printed with 0.1 mm and 0.15 mm layer thicknesses.

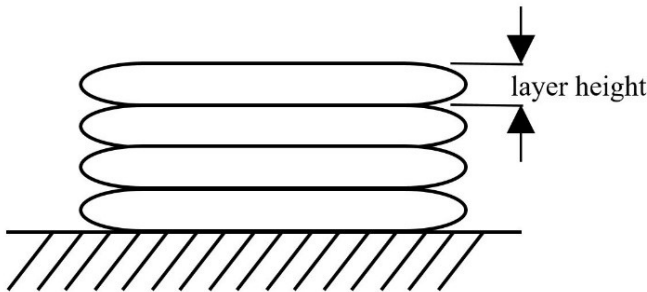


Figure 4. Illustration of layer height.

## Part Orientation

Energy consumption is directly related to the part's orientation on the build plate for two reasons. First, a part's orientation determines the amount of support material needed under the overhang and bridge features. Thus, total material extrusion, extrusion time, and related energy usage depend on the part's orientation. Second, the shape of each printed layer is the cross-sectional geometry of the part at that level. Thus, the G-code for each layer and the related printing parameters—such as the printing path and the travel speed of the printer head—change as the part's orientation on the build plate changes. However, a part can be oriented in an infinite number of ways on the build plate, making it impossible to measure the effects of orientation on energy con-

sumption. Moreover, a part must be printed, debound, and sintered in the most stable orientation in order to achieve the best dimensional control and mechanical characteristics. Thus, when analyzing the effects of orientation, the shape of the test part is designed in a way that the stability of the part and the amount of support structures are not affected by the orientation. For these reasons, the rectangular block design without any internal, bridge, or overhang structures is an ideal shape. Figure 5 shows the two orientations, flat and upright, used for the experimental printing.

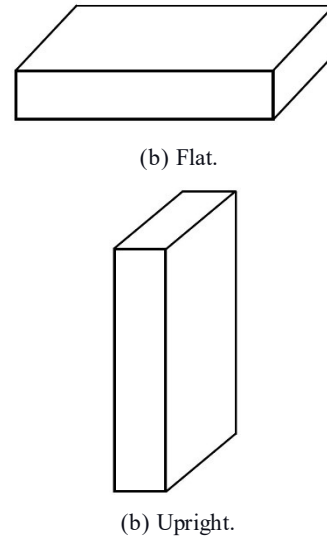


Figure 5. Illustration of part orientations.

## Print Pattern

As mentioned previously, the G-code or the print trajectory of each layer determines the printing speed, total print time, and sometimes the amount of material usage, thereby affecting energy usage. Fabricate software controls the print trajectory through the parameter "print pattern." Figure 6 shows how, for this parameter, "Lines" and "Concentric" print patterns were studied.

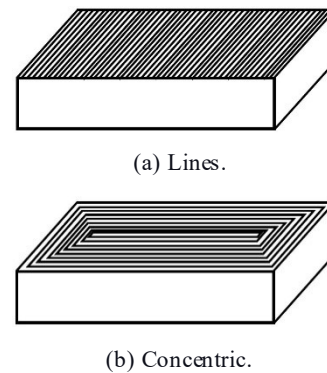


Figure 6. Illustration of print patterns.

After the parts were 3D printed, they were placed in a tank in the debinding unit for chemically solving the primary binder. The tank was filled automatically with a mixture of trans-Acetylene dichloride and a proprietary material. The amount of the solvent mix depends on the total mass of the parts placed into the tank. The debinding process was completed in seven steps: filling the tank, calibrating, heating, debinding, distillation, draining, and drying. Chemical debinding took place at 44°C; after the debinder was drained, the parts were dried at 70°C. The Fabricate software calculated the length of each step during model preparation. The capacity of the tank was 3.5 kilograms, and multiple parts could be debound at the same time.

Even though the debinder had a 3.5-kilogram debinding capacity, the length of the debinding step depends on the thickest part in the tank. The estimated time to debind the largest printable solid sphere (a 3 kg sphere with 100% infill) was 2563 hours. However, the debinder's maximum debinding time limit was 288 hours. The largest solid sphere that could be debound in 288 hours would have a diameter of 25.3 mm and weigh 63.7 grams. Figure 7 shows how the debinding step was analyzed through three spheres with 1, 2, and 4 mm diameters.



Figure 7. Spherical test part with 2 mm diameter.

## Sintering

The last phase was completed in the Studio sintering furnace. At this stage, brown parts still had the backbone plastic binder and 20%-30% primary binder. The furnace performed two major tasks: thermal debinding of the remaining binders and sintering of the metal particles. After the parts were placed into the furnace, the furnace chamber was closed and the partial pressure atmosphere was created with the help of a vacuum pump. Before the thermal debinding starts, a 97% argon + 3% hydrogen gas mix was pumped into the chamber. The gas mix had two roles: 1) during the thermal debinding stage, the gas flow carries the evaporated binder particles away; and, 2) during the sintering stage, hydrogen reacts with the oxygen in the furnace and on the surface of the metal and reduces it. These two functions keep the metal part purer and denser. The load capacity of the furnace was 3 kg.

## Results

The Desktop Metal Studio 3D printer ran on a single-phase circuit with 100-130 VAC, 50-60 Hz, and 15A ratings. For measuring the power consumption of the equipment, a line splitter was placed between the power plug and the wall outlet. Measurements were recorded every second. Data were collected according to the experimental design for three parameters at two levels, requiring eight experimental runs (2<sup>3</sup>):

1. Layer height: 0.1 mm vs. 0.15 mm
2. Part orientation: flat vs. upright
3. Print pattern: lines vs. concentric

The eight experiments were randomized and repeated three times each in order to minimize any hidden effects and improve the reliability of the results. Thus, twenty-four total experimental runs were carried out. Figure 8 shows a typical print job, which consists of calibration, printing the raft, printing the interface, printing the part, material auto load, and cooling stages. The auto load takes place only if the material in the extruder head is finished during the printing stage. If there is enough material available in the extruder head for the printing stage, auto load does not occur. As for printing of the raft and interface features, the size of these two features heavily depends on the cross-sectional shape of the first layer of the part. Thus, part orientation affects the amount of energy usage through the size of the raft and interface features. For these reasons, two measures were developed for the comparative analysis of the experimental runs. The first measure was the “piece” energy, or the amount of energy used during part printing only. The second measure was the “total” energy, or the total amount of energy consumed during the printing job, including all stages except the auto load. Figure 8 also shows that a typical run for printing a test part took less than two hours, and that the power requirement ranged between 0.2 kVA and 0.4 kVA. Table 1 shows a summary of the results of the experimental runs.

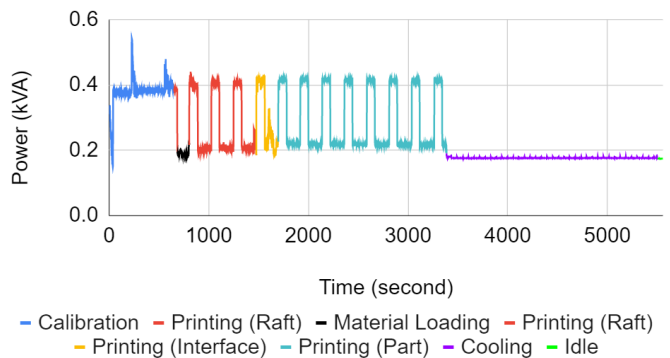


Figure 8. Power levels during 3D printing.

In order to understand the main effect of a single parameter and parameter interactions, interaction charts were created from the data of Table 1. Figure 9 shows interactions

between layer height and print pattern. It is clear that at all combinations of layer height and print pattern parameters, the “Upright” part orientation caused more energy consumption compared to the “Flat” part orientation.

Table 1. Average consumption of energy and material during experimental runs.

Runs	Layer height (mm)	Part orientation	Print pattern	Piece energy (kwh)	Total energy (kwh)	Piece material (g)	Total material (g)
1	0.10	Flat	Concentric	0.133	0.383	7.48	17.32
2	0.15	Flat	Concentric	0.093	0.330	7.6	18.36
3	0.10	Flat	Lines	0.142	0.378	7.48	18.06
4	0.15	Flat	Lines	0.098	0.336	7.61	18.37
5	0.10	Upright	Concentric	0.198	0.414	7.5	11.99
6	0.15	Upright	Concentric	0.132	0.342	7.5	12.04
7	0.10	Upright	Lines	0.206	0.417	7.52	12.01
8	0.15	Upright	Lines	0.141	0.352	7.52	12.06

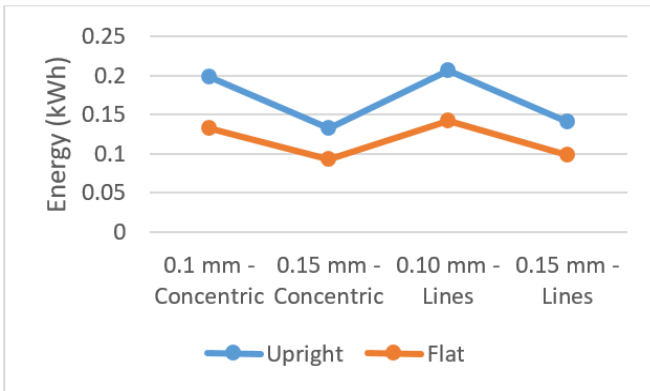


Figure 9. Effect of part orientation on energy consumption (Upright vs. Flat).

Figure 10, the interaction chart for part orientation and print pattern, presents the effect of “layer height” on energy consumption. According to Figure 10, when all other parameters are kept constant, the 0.10 mm layer height used more energy than the 0.15 mm layer height print setting. Looking at the data from Figure 11, the analysis on the print pattern did not yield a significant difference, except for the 0.10 mm – Upright print settings; however, it can be concluded that the “Lines” print pattern was associated with higher energy consumption. The Desktop Metal Studio debinder (100-130 VAC, 50-60 Hz, and 15A ratings) was used to measure the power consumption of the debinder with a Fluke power logger; a special extension cord with split lines was built by the school technician. Measurements were recorded every second. The primary parameter for the debinding process was the thickness of the part to be de-

bound. The thickest section of the part determined the debinding time, which was also correlated with energy consumption. Since the debinding process was not affected by the previously defined print parameters (layer height, print pattern, and part orientations) and all rectangular test parts had the same shape, three spherical test parts were created with 1, 2, and 4 mm diameters. Figure 12 shows the energy consumption of the debinder during the debinding process of the spherical test part with a 1 mm diameter. The debinding cycle for the test part was completed in thirteen hours and forty-one minutes. As seen from Figure 12, in a typical debinding cycle, the primary energy-consuming steps were initial heating, debinding, drying, and distillation.

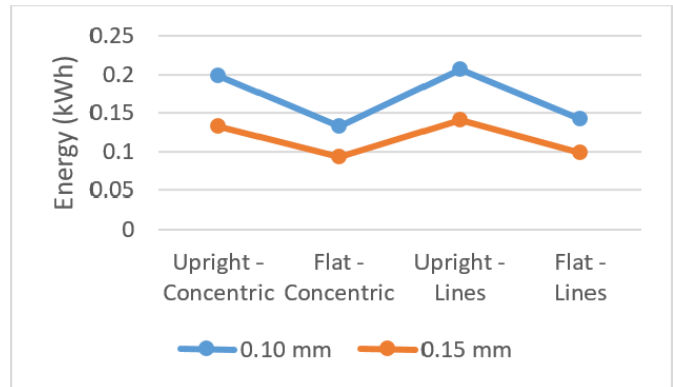


Figure 10. Effect of layer height on energy consumption (0.10 mm vs. 0.15 mm).

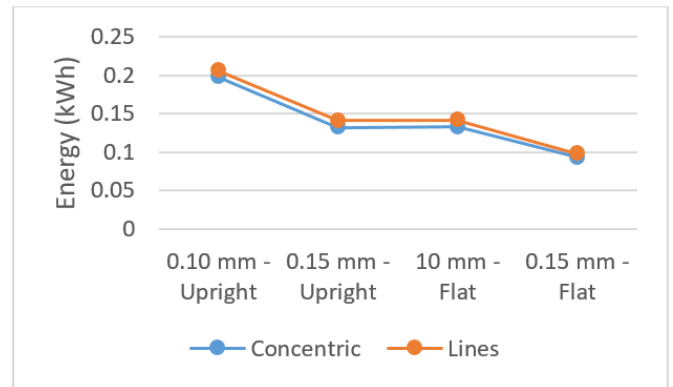


Figure 11. Effect of print pattern on energy consumption (Concentric vs. Lines).

Table 2 presents the parameters of the three test runs and their corresponding energy consumption. The analysis of the debinding process showed that the thickness of the part had a significant effect on energy consumption, and the only step affected by the thickness was debinding. Even though the distillation step was one of the major energy-consuming steps, it was affected by the amount of material debound rather than the part thickness. Thus, the distillation step had no significant effect on the difference between the total energy requirements of the test runs.

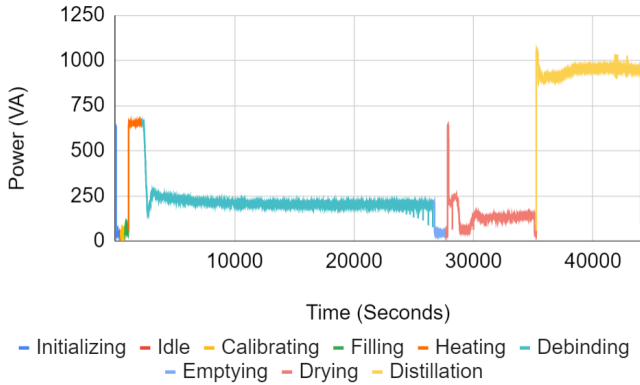


Figure 12. Power levels during debinding.

Table 2. Energy consumption during debinding test runs.

Runs	1	2	3
Final diameter (mm)	1	2	4
Printed diameter (mm)	1.2	2.4	4.8
Total energy (kWh)	4.585	4.756	5.230

The Desktop Metal Studio sintering furnace ran on a 3-phase delta circuit with 208 VAC, 60 Hz, 30A/phase ratings. For measuring the power consumption of the furnace, magnetic probes were hooked up to the circuit from the safety switch. Measurements were recorded every thirty seconds. The maximum sintering capacity of the furnace was 3 kg. It would be wiser to load the furnace with parts closer to the maximum capacity for better efficiency in an industrial setting. In this study, the furnace was loaded with parts of various shapes and weights totaling 2.759 kg. The sintering process consisted of initialization, thermal debinding, sintering, and cooling steps; it took forty-one hours and fifteen minutes to complete. The power requirement ranged between 0.2 kW and 6.2 kW. Figure 13 shows that, for the test run, the sintering furnace consumed 70.661 kWh energy.

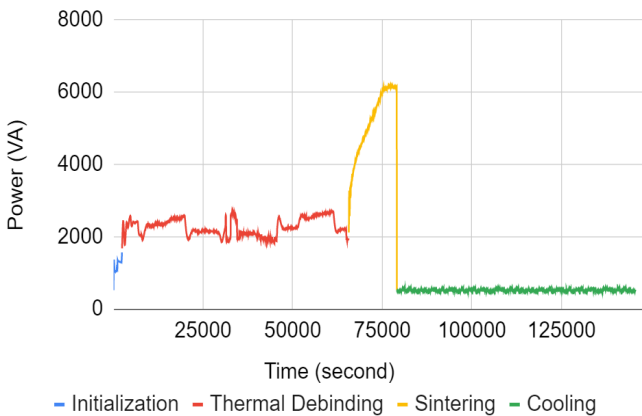


Figure 13. Power levels during sintering.

## Discussion

Layer height, part orientation, and print pattern are known to affect energy consumption significantly. In this regard, the test results for the 3D printing stage were consistent with previous research conducted on FDM systems. This current study showed that the raft, a consumable feature, also significantly affected the total energy requirement for the printing stage. For the BDM system, the raft could not be turned off, as it was a functional feature; that is, it provided a level surface, better adhesion, and better stability throughout the printing, debinding, and sintering sequence. However, the shape and size of the raft could not be modified to control energy consumption. The shape and size of the raft were functions of the part printing orientation, which depended on factors such as part stability, material consumption, and surface quality. For example, printing a rectangular object on its smallest face resulted in a smaller raft and thereby less energy usage, but the maximum recommended height-to-width ratio for the BMD system was 8:1. If the printed part exceeded that ratio, it would slump and collapse.

The 3D printer auto load feature was also a significant part of the 3D printing stage that took place when a material rod was consumed after 21 grams of material usage. The auto load activity lasted two minutes and required 0.019 kWh of energy. The debinder's energy consumption profile heavily depended on part thickness. The maximum allowable debinding time was 12 days. A solid sphere with a 25.3 mm diameter was the thickest object that could be debound with an estimated debinding time of 289 hours and 41 minutes, and an energy consumption of 63.6 kWh. Since the material thickness was the most significant parameter for the debinding time and energy usage, it would be more cost-effective to debind parts with similar thicknesses in the same debinding cycle with a maximum load. Furnace operation was not sensitive to previously mentioned part characteristics and parameters. Moreover, the furnace load capacity was 3 kg and, at each cycle, it consumed 750L of furnace gas. From an economic point of view, it makes more sense to always run the furnace at full capacity.

From the experimental runs, the SEC was calculated for each stage separately. For the 3D printing process, the piece only SEC varied between 12.9 kWh/kg and 28.1 kWh/kg; whereas, when printing of the raft, interface, and auto load processes are included, the SEC varied between 18.7 kWh/kg and 35.4 kWh/kg. For both situations, the lowest SEC was achieved when the part was printed at a layer thickness of 0.15 mm in the flat orientation with a concentric print pattern, and the highest SEC was calculated when the part was printed at a layer thickness of 0.10 mm in the upright orientation with the lines print pattern. The SEC for the sintering process was calculated as 25.6 kWh/kg. The SEC for the debinding process depended on the thickness of the thickest feature. When the thickness was 25.3 mm, the maximum allowed debinding time was reached and, at this

point, the SEC was 17.8 kWh/kg, whereas when the thickness of the thickest section on the part was 1 mm, the SEC was calculated to be 1.31 kWh/kg. The infill density (infill material percentage) was not investigated for its effect on energy consumption, because all test models were prepared with a “Standard+” printing profile, which fills the inside of the part completely. This profile generated parts with 96%-99.8% relative density comparable to the parts produced through other manufacturing processes, such as metal injection molding (MIM), casting and machining in terms of their relative densities.

## Conclusions

Additive manufacturing has become one of the prevailing advanced manufacturing processes, due to its unique production capabilities. Recent developments in metal 3D printing technologies have made it possible to create industrial-grade parts from ferrous and non-ferrous metals. Low volume production, custom design, on-demand production, inventory minimization, and distributed manufacturing are a few of the promising advantages of these technologies from a business point of view. Studying all aspects of 3D printing technologies, including cost, environmental safety, human health, quality, and sustainability, is imperative in order to better understand the opportunities and risks associated with these technologies. In this current study, energy requirements of the BMD additive manufacturing technology were analyzed, significant parameters were identified, and the advantages and limitations of the technology were discussed. The authors hope that this paper will serve as a valuable resource for future research on the environmental, financial, and social sustainability of metal 3D printing technologies.

## References

- Baumers, M., Tuck, C., Hague, R., Ashcroft, I., & Wildman, R. (2010). A comparative study of metallic additive manufacturing power consumption. *Solid freeform fabrication symposium*, 2009, 278-288.
- Baumers, M., Tuck, C., Bourell, D. L., Sreenivasan, R., & Hague, R. (2011). Sustainability of additive manufacturing: measuring the energy consumption of the laser sintering process. *Proceedings of the Institution of Mechanical Engineers, Part B: Journal of Engineering Manufacture*, 225(12), 2228-2239.
- Baumers, M., Tuck, C., Wildman, R., Ashcroft, I., & Hague, R. (2011). Energy inputs to additive manufacturing: does capacity utilization matter. *Eos*, 1000(270), 30-40.
- Bourell, D., Coholich, J., Chalancon, A., & Bhat, A. (2017). Evaluation of energy density measures and validation for powder bed fusion of polyamide. *CIRP Annals*, 66(1), 217-220.
- Dahmus, J. B., Gutowski, T. G., (2004). An environmental analysis of machining, in: 2004 ASME International Mechanical Engineering Congress and Exposition, IMECE 2004, November 13, 2004 - November 19, 2004, American Society of Mechanical Engineers, Manufacturing Engineering Division, MED. American Society of Mechanical Engineers, pp. 643-652. doi:10.1115/IMECE2004-62600
- Faludi, J., Baumers, M., Maskery, I., & Hague, R. (2017). Environmental impacts of selective laser melting: do printer, powder, or power dominate? *Journal of Industrial Ecology*, 21(S1), S144-S156.
- Griffiths, C. A., Howarth, J., De Almeida-Rowbotham, G., Rees, A., & Kerton, R. (2016). A design of experiments approach for the optimisation of energy and waste during the production of parts manufactured by 3D printing. *Journal of cleaner production*, 139, 74-85.
- He, Y., Liu, F., Wu, T., Zhong, F.-P., Peng, B. (2012). Analysis and estimation of energy consumption for numerical control machining. *Proceedings of the Institution of Mechanical Engineers, Part B: Journal of Engineering Manufacture*, 226, 255-266. doi:10.1177/0954405411417673
- Jackson, M. A., Van Asten, A., Morrow, J. D., Min, S., & Pfefferkorn, F. E. (2016). A comparison of energy consumption in wire-based and powder-based additive-subtractive manufacturing. *Procedia Manufacturing*, 5, 989-1005.
- Junk, S., & Côté, S. (2012). A practical approach to comparing energy effectiveness of rapid prototyping technologies. *Proceedings of AEPR*, 12, 12-14.
- Kara, S., & Li, W. (2011). Unit process energy consumption models for material removal processes. *CIRP Annals – Manufacturing Technology*, 60(1), 37-40. doi:10.1016/j.cirp.2011.03.018
- Kellens, K., Dewulf, W., Deprez, W., Yasa, E., & Dufloy, J. (2010). Environmental analysis of SLM and SLS manufacturing processes. *Proceedings of LCE2010 Conference*, pp. 423-428.
- Kellens, K., Yasa, E., Dewulf, W., & Dufloy, J. R. (2010). Environmental assessment of selective laser melting and selective laser sintering. *Methodology*, 4(5).
- Kellens, K., Yasa, E., Renaldi, R., Dewulf, W., Kruth, J. P., & Dufloy, J. (2011). Energy and resource efficiency of SLS/SLM processes (keynote paper). *SFF Symposium 2011*, pp. 1-16.
- Kellens, K., Mertens, R., Paraskevas, D., Dewulf, W., & Dufloy, J. R. (2017). Environmental Impact of Additive Manufacturing Processes: Does AM contribute to a more sustainable way of part manufacturing? *Procedia Cirp*, 61, 582-587.
- Liu, Z. Y., Li, C., Fang, X. Y., & Guo, Y. B. (2018). Energy consumption in additive manufacturing of metal parts. *Procedia Manufacturing*, 26, 834-845.
- Luo, Y., Ji, Z., Leu, M. C., & Caudill, R. (1999). Environmental performance analysis of solid freedom fabrication processes. *Proceedings of the 1999 IEEE international symposium on electronics and the environment (Cat. No. 99CH36357)* (pp. 1-6). IEEE.

- 
- Morrow, W. R., Qi, H., Kim, I., Mazumder, J., & Skerlos, S. J. (2007). Environmental aspects of laser-based and conventional tool and die manufacturing. *Journal of Cleaner Production*, 15(10), 932-943.
- Paris, H., Mokhtarian, H., Coatană, E., Museau, M., & Ituarte, I. F. (2016). Comparative environmental impacts of additive and subtractive manufacturing technologies. *CIRP Annals*, 65(1), 29-32.
- Sachs, E., Cima, M., & Cornie, J. (1990). Three-dimensional printing: rapid tooling and prototypes directly from a CAD model. *CIRP Annals*, 39(1), 201-204.
- Sreenivasan, R., & Bourell, D. (2010). Sustainability Study in Selective Laser Sintering- An Energy Perspective. *Minerals, Metals and Materials Society/AIME, 420 Commonwealth Dr., P. O. Box 430 Warrendale PA 15086 USA*. [np]. 14-18 Feb.
- U.S. EIA, *Electric Power Annual*. (2019). Retrieved from <https://www.eia.gov/electricity/annual/pdf/epa.pdf>
- Wilson, J. M., Piya, C., Shin, Y. C., Zhao, F., & Ramani, K. (2014). Remanufacturing of turbine blades by laser direct deposition with its energy and environmental impact analysis. *Journal of Cleaner Production*, 80, 170-178.
- Yoon, H. S., Lee, J. Y., Kim, H. S., Kim, M. S., Kim, E. S., Shin, Y. J. ...Ahn, S. H. (2014). A comparison of energy consumption in bulk forming, subtractive, and additive processes: Review and case study. *International Journal of Precision Engineering and Manufacturing-Green Technology*, 1(3), 261-279.

## Biographies

**MEHMET EMRE BAHADIR** is an assistant professor of industrial technology at Southeastern Louisiana University. He earned his BS in Industrial Engineering from Marmara University in 2001, MA in Technology in 2003 from the University of Northern Iowa, and doctoral degree in technology in 2009 from the University of Northern Iowa. Dr. Bahadir's research interests include environmental sustainability, lifecycle assessment, discrete system simulation, and GD&T. Dr. Bahadir may be reached at [mehmet.bahadir@southeastern.edu](mailto:mehmet.bahadir@southeastern.edu)

**CALEB LAGARRIGUE** is a BIM/AutoCAD Design Coordinator at PSX Worldwide Audiovisual Technologies. He earned his BS in Mechanical Engineering Technology from Southeastern Louisiana University in 2021. Caleb's research interests include the environmental impact of certain manufacturing technologies. Caleb may be reached at [lagarrigue.caleb@yahoo.com](mailto:lagarrigue.caleb@yahoo.com)

**JUAN GONZALEZ** is an electrical designer at Pike Electric. He earned his BS in Electrical Engineering Technology from Southeastern Louisiana University in 2021. Juan's research interests include electrical circuitry and components, as well as additive manufacturing technology. Juan may be reached at [juangonzalez21899@yahoo.com](mailto:juangonzalez21899@yahoo.com)

# INNOVATIVE AUGMENTED REALITY APPLICATION FOR EFFECTIVE UTILIZATION OF HAZARD COMMUNICATION PICTOGRAMS

Ulan Dakeev, Sam Houston State University; Ali Aljaroudi, Sam Houston State University

## Abstract

Hazardous chemicals are present in many workplaces. For that reason, hazardous communication regulations were established for safety assurance for facilities, workers, and their surrounding environments. The objective of this study was to investigate the effectiveness of the AR\_GHS (augmented reality, globally harmonized system) for non-English speaking employees in order to enhance safety awareness of GHS pictograms. The results of the Wilcoxon test showed that the participant scores significantly increased after using the AR application ( $P < 0.01$ ). The study results also showed that utilizing the AR app could enhance understanding of the GHS pictograms for non-English speaking janitorial staff, which could contribute to their safety awareness of hazardous materials.

## Introduction

In many workplaces, hazardous chemicals are needed and kept on site for the completion of different types of tasks. Globally, a set of hazardous communication (HAZCOM) regulations and standards were established to ensure that these chemicals could be used safely not only for the facilities but also the workers and the surrounding environment (OSHA, 2005; UNECE, 2019). The U.S. Occupational Safety and Health Administration (OSHA) and the United Nations Economic Commission for Europe (UNECE) evaluated the effectiveness of a communication system inform workers of hazards to which they could be exposed and of which companies had knowledge. Thus began the movement that became known as the right-to-know movement, along with regulations requiring safety data sheets (SDSs) and labeling for hazardous materials to which employees or the public might be exposed. Information systems that proliferate knowledge of these hazards can mitigate related risks (OSHA, 2020).

OSHA issued a rule in 2012 to modify the Hazard Communications Standard to adopt the United Nations' version of the GHS for the labeling of chemicals (OSHA, 2019). This modification would improve the quality and consistency of information provided to employers and workers regarding safety awareness and protective measures (Boelhouwer, Davis, Franco-Watkins, Dorris, & Lungu, 2013; OSHA, 2020). Unlike other occupations, where the employees communicate in a common language, janitorial staff in the U.S. are diverse and may not speak English as their first language. Additionally, the companies may not conduct health training for janitorial staff to avoid training

costs. Training programs are underused for tackling this problem. Regular in-depth training may provide an opportunity to raise pay, enhance skills and job performance, help with turnover, and show that management cares about their workers. The budget is often the core power in training decisions. Many organizations do not appreciate the value of training materials when they look at them on paper.

The main focus of the UN and OSHA, providing an effective HAZCOM program by standardizing hazard pictograms, is facing a major challenge; that is, effective training provided to the workers, especially janitors/custodians. Cleaning is a core factor in public health. However, the role of the janitors often has a negative perception, not only by building occupants but also by the janitors themselves. Janitors (or custodians) are among the occupations reporting the highest rates of work-related asthma (Jaakkola, Piipari, & Jaakkola, 2003). There is also a high risk coming from the improper mixing of chemicals and slip-and-fall incidents, not to mention the negative impact on public health if cleaning services are completed incorrectly.

Despite these risks, janitors play a major role in maintaining the health of building occupants. They contribute to preventing the spread of illness and infection and protect the health of the indoor environment. Unlike Europe, there are no minimum educational degree requirements for becoming a janitor in the U.S. Another problem is low pay. The U.S. Bureau of Labor Statistics (BLS) reported that the median pay for janitors was around \$26,110 per year and \$12.55 per hour in 2018 (BLS, 2018).

## Literature Review

The manufacturing industry is acutely aware of the impact that poor job site communication can have on worker safety behaviors. The BLS (2012) estimated that there were 705,000 to 2.2 million Hispanic workers between 1990 and 2010. The National Center for Farmworker Health (NCFH) reported that 72% out of three million migrant and seasonal farmworkers living and working in the U.S. are foreign-born (NCFH, 2012). OSHA also estimated that there were over 945,000 hazardous chemical products in the workplace that could affect worker safety (OSHA, 2006). Moreover, the BLS estimated that 2,384,000 janitors were employed in 2016, placing them at 2.7 times the risk of all other occupations (BLS, 2016). Charles, Loomis, and Demissie (2009) reported that janitors are at risk of respiratory diseases, dermatologic illnesses, psychosocial stressors, mental disorders, infectious diseases, and musculoskeletal disorders.

According to the NCFH, 95% of foreign-born janitorial workers were born in Mexico, 4% were born in Central American countries, and 1% were born elsewhere (NCFH, 2012). Therefore, it is crucial to deliver comprehensive education of GHS pictograms to non-English speaking employees—such as janitorial staff, carpenters, etc.—that are typically neglected during hazardous sign training. To enhance janitorial awareness of their safety and health in the manufacturing industry, a computer-based AR simulation called AR\_GHS was developed and tested in non-English speaking countries in order to assess the understanding of safety pictograms at job sites. This simulation was developed by the authors of this study and is available through Google Play market. Key learning objectives included participating in and understanding what GHS pictograms represent and the potentially hazardous impacts on human health. The purpose of this study was to investigate whether or not there is a difference in the comprehension of information presented in GHS pictograms and the AR\_GHS for non-English speakers.

## Methodology

Figure 1 shows the AR\_GHS safety tool that was developed for employee awareness and/or training on OSHA's nine pictograms. Employee awareness of pictograms requires workers to retrieve and understand potential hazards that are present in their proximity (OSHA, 2021), as he/she performs janitorial tasks on the premises. Assembly of these OSHA-determined pictograms was selected, since these pictograms have been internationalized and are present in almost all manufacturing companies.



Figure 1. Internationally standardized GHS pictograms.

To develop the AR\_GHS safety tool, the detailed image targets were analyzed and recognizable algorithmic anchors were placed for camera detection. A prominent image target can only be appropriately utilized if the algorithm can process 80% of the data. For this purpose, the Vuforia image processing algorithm was selected to analyze each of the pictograms to be used in the AR application. To develop the AR tool, the researchers generated a 2D animation using Photoshop, imported the animation into the Unity software, and scripted it in the C# programming language.

The input to the developed AR tool was 1) GHS pictogram (see again Figure 1) detection and 2) real-world context in the form of a 2D animation (see Figure 2). When the worker is ready to visualize the pictogram, he/she can open the AR\_GHS safety tool on their device, (i.e., phone or tablet running Android on an iOS platform) and point the device's camera at the GHS pictogram. Figure 2 shows how the camera will demonstrate an overlaid animation.



Figure 2. Overlaid animation on AR\_GHS tool.

The GHS pictograms were randomly placed in an open area for the participants to visualize and recognize the hazards represented by the pictograms. Comparative statistical analyses were conducted for a group of volunteer participants supervised by the researchers—a demo video of the application can be seen via the link provided by Dakeev (2021). For the procedure, a total of 71 untrained janitorial and carpentry workers (aged 18-45, male=51, female=20) participated in the study from two countries (Nigeria, and Kyrgyzstan). None of these employees were certified janitorial staff, but rather regular employees of the organizations. Although some of the employees had undergraduate degrees, they were either retired or were ineligible to work, due to personal restrictions. None of the participants received any prior official OSHA or local safety-related training on hazardous materials. Two independent groups were randomly recruited to participate in the study. The GHS pictograms were printed out and posted on the wall, where the first group was invited to observe and study the pictograms and fill out a brief survey prepared by the researchers. The rooms, where the participants conducted their experimental study, was an empty room with a regular table and a chair. A similar setting was used in both countries.

The second group was never exposed to the pictograms, but rather was invited into the room with the pictograms. The participants were given an android device with the AR application installed and asked to point the camera of the device at the pictograms (see again Figure 2). After completion, the group-2 participants were asked to fill out the survey. The answers were recorded for both pretest and posttest analysis of the AR application. An independent sample t-test was conducted to observe preliminary report between genders.

All statistical analyses were completed using SPSS Statistics 25.0. Table 1 shows all of the pre- and post-test scores, first calculated as mean and standard deviations for each individual subject, based on gender and geographical location. A pairwise comparison statistical analysis was conducted in order to examine the effectiveness of the AR app in enhancing the participants' understanding of the GHS pictogram. A Shapiro-Wilk test was conducted in each one of the four datasets to test the normality of data frequency. If the data passed the normality test ( $P > 0.05$ ), a t-test should be used. If the normality was violated ( $P < 0.05$ ), a non-parametric Wilcoxon statistical test should be used. Independent analysis was conducted to investigate the influence of gender/geographical location differences in understanding the GHS pictograms, using the AR tool in future studies.

Table 1. Descriptive statistics for participants.

Correct Scores	Pre-	Post-
Nigeria	2.57 ± 1.27	5.85 ± 0.89
Kyrgyzstan	2.92 ± 1.14	5.86 ± 1.03
Male	2.81 ± 0.98	6.18 ± 0.75
Female	2.80 ± 1.39	5.50 ± 1.08
Overall	2.80 ± 1.17	5.86 ± 0.96

## Results

Table 1 summarizes the correct scores as descriptive statistics (mean ± standard deviation [SD]) of the study population. Based on the Shapiro-Wilk test, the normality of data frequency was violated for pre- ( $P = 0.01$ ) and post- ( $P < 0.01$ ) data. Therefore, a non-parametric statistical test (Wilcoxon test) was used to analyze the data. The results of the Wilcoxon test showed that the participants' scores increased significantly after using the AR app ( $P < 0.01$ ). The independent test showed that there was no significant influence of gender differences ( $P = 0.10$ ) or geographical location ( $P = 0.15$ ).

## Conclusions

The preliminary study results showed that the innovative augmented reality (AR) application could enhance the

understanding of the GHS pictograms for non-English speaking employees as well as contribute to their safety awareness of hazardous materials. Further collection of data is necessary to both validate these important discoveries as well as study additional variables that AR technology can introduce to improve safety. The main limitation of this study was the sample size. A follow-up research study is essential for assessing more subjects from more geographical locations. Therefore, additional countries such as Russia, Georgia, Mexico, and Turkey are under observation to report further results in the future.

## References

- Boelhouwer, E., Davis, J., Franco-Watkins, A., Dorris, N., & Lungu, C. (2013). Comprehension of hazard communication: Effects of pictograms on safety data sheets and labels. *Journal of Safety Research*. <https://doi.org/10.1016/j.jsr.2013.06.001>
- Bureau of Labor Statistics. (2018). *Occupational Employment and Wages*. BLS, 2018.
- Bureau of Labor Statistics. (2012). *Occupational Employment and Wages*. BLS, 2012.
- Bureau of Labor Statistics. (2016). *Nonfatal Occupational Injuries and Illnesses: Cases with days of job transfer or restriction*. BLS, 2016.
- Charles, L. E., Loomis, D., & Demissie, Z. (2009). Occupational hazards experienced by cleaning workers and janitors: a review of the epidemiologic literature. *Europe PMC*, 34(1), 105-116.
- Dakeev, U. (2021). *AR GHS App Demo*. Retrieved from [https://www.youtube.com/watch?v=ykhzbv08q-E&ab\\_channel=SilfGenson](https://www.youtube.com/watch?v=ykhzbv08q-E&ab_channel=SilfGenson)
- Jaakkola, K., Piipari, R., & Jaakkola, M. S. (2003) Occupation and asthma: a population-based incident case-control study. *American Journal of Epidemiology*, 158, 981-987.
- National Center for Farmworker Health. (2012). *Farmworkers' Health Fact Sheet, Data from the National Agricultural Workers Survey*. NCFH, 2012.
- Occupational Safety and Health Administration. (2020). *Hazard communication standard. Final rules*. OSHA, 2020.
- Occupational Safety and Health Administration. (2006). Occupational Safety and Health Standards. *Hazard Communication, 1910*, 1200.
- Occupational Safety and Health Administration. (2021). *Hazard Communication Standard: Labels and Pictograms*. OSHA, 2021.
- Occupational Safety and Health Administration. (2005). *Hazard communication standard. Final rules*. OSHA, 2005.
- United Nations Economic Commission for Europe. (2019). *Globally Harmonized System of Classification and Labelling*. UNECE, 2019.

---

## Biographies

**ULAN DAKEEV** is an assistant professor of engineering technology at Sam Houston State University. He earned his BS in Industrial Engineering from the International Black Sea University in 2004, MS in Industrial Management from the University of Northern Iowa in 2011, and PhD in Technology from the University of Northern Iowa in 2013. Dr. Dakeev's research interests include student engagement and motivation, and virtual and augmented reality. Dr. Dakeev may be reached at [dakeev@shsu.edu](mailto:dakeev@shsu.edu)

**ALI ALJAROUDI** is an assistant professor of engineering technology / safety management at Sam Houston State University. He holds a BS degree in industrial systems engineering from King Fahd University of Petroleum and Minerals, an MS degree in occupational safety and health from Murray State University, and a PhD degree in occupational safety and ergonomics from the University of Cincinnati. Dr. Aljaroudi's main research interests include behavioral-based safety, physical ergonomics, thermal stress, work physiology, and occupational safety and health. Dr. Aljaroudi may be reached at [axa220@shsu.edu](mailto:axa220@shsu.edu)

# DIFFERENCE IN RESPONSE OF A 40-STORY, BUCKLING RESTRAINT-BRACED FRAME STRUCTURE WITH FLEXIBLE DIAPHRAGM

Mohammad T. Bhuiyan, West Virginia State University

## Abstract

The floor systems of buildings play an important role in distributing horizontal forces among vertical, lateral load-carrying elements. It is a customary in structural engineering practice to assume rigid diaphragm constraints when modeling floors for lateral force analyses of building structures. It is generally understood that building structures with flexible diaphragms behave differently from systems with rigid diaphragms. The practice of assuming rigid diaphragm may not necessarily be conservative. In the past, studies have been carried out, predominantly for low-rise buildings, to look for differences in response if floors were modeled as having a flexible diaphragm rather than a rigid one. Bhuiyan and Leon (2013) studied this different behavior for a diagrid tall building. The objective of this current article is to evaluate the effect of diaphragm flexibility on the structural response of a 40-story, buckling restraint-braced (BRB) frame structure. A detailed model of the floor system, including all primary structural members, was constructed. The author found that the structure modeled with a flexible diaphragm could experience significantly higher accelerations and moderate differences in displacement. Deformation-demand capacity ratio for many braces were found to be around 10% higher with a flexible diaphragm.

## Introduction

While performing time-history analyses, designers and researchers come across some crucial modeling questions, such as, whether the assumption to model the building floor plates with a rigid diaphragm option is satisfactory. The concept that building structures with flexible diaphragms behave differently from systems with rigid diaphragms is fundamental. The vast majority of engineers assume a rigid diaphragm constraint for modeling floors for 3D, non-linear, time-history analyses. Bhuiyan and Leon (2013) found that, a steel diagrid tall building modeled with flexible diaphragms can experience higher accelerations and displacements than structures modeled with rigid diaphragms, and that their fundamental periods of vibration can be noticeably longer.

Basu and Jain (2004) studied a three-story, asymmetric, concrete shear wall building with a width-to-length ratio of 1:5. They studied the effect of a flexible diaphragm on this asymmetric building. They concluded with the following statement.

It is seen that treating the diaphragms of such buildings as rigid for torsional analysis may cause considerable error. The example also illustrates that the contribution of accidental torsion as well as the torsional amplification terms can be quite significant. (p.1175)

Tena-Colunga and Abrams (1996) studied the seismic response of three structures with flexible diaphragms: 1) a two-story firehouse in Gilroy with unreinforced masonry walls; 2) a two-story timber office building in Palo Alto with grouted and reinforced clay-unit masonry shear walls; and, 3) an eight-story hotel in Oakland with unreinforced clay-unit masonry and reinforced-concrete shear walls. They noted that

...as diaphragm flexibility increases, diaphragm and shear-wall acceleration can increase in some cases. Flexible in-plane shear walls can vibrate at higher accelerations than stiffer walls in a flexible-diaphragm system. Design criteria based on rigid-diaphragm behavior is not necessarily conservative for flexible-diaphragm systems. (p.444)

Barron and Hueste (2004) studied reinforced concrete shear wall buildings with aspect ratios of 2:1 and 3:1 and heights of three and five stories. They stated that, "for almost all analyses of the case study buildings, a flexible diaphragm model produces more frame displacement and inter-story drift than a rigid diaphragm model. This is especially evident for frames that are closer to the middle of the building." Fang (2015) studied the seismic behavior of steel structures with semi-rigid diaphragms. His case study structures were four stories high with an aspect ratio of 1:3. He noted that

The 3D model with elastic shell elements overestimates the ultimate strength and post-buckling strength: According to the analytical results in the one-story 3D model, both ultimate strength and post-buckling stiffness are higher than the other three cases (i. bare frame with axial restraint, ii. Composite frame with axial restraint, and iii. Composite frame). However, the results show that the structure is very sensitive to the modeling of diaphragm: the development of shell element capable of tracking the strength and stiffness degradation of diaphragm is needed. (p.100)

Past studies on this topic were predominantly done for low-rise buildings. Also, not many studies were performed on steel buildings, especially high-rise buildings. The objective of this current study was to evaluate the effect of diaphragm flexibility on the structural response of a 40-story, buckling restraint-braced frame building.

## Buckling-Restrained Braced Frames

The following quote is from the government website for the National Institute of Standards and Technology (NIST, 2015).

Buckling-restrained braced frames (BRBFs) is one of a number of newer types of seismic force-resisting systems used in modern building designs. The two example configurations of Figure 1 illustrate that BRBFs resist lateral loads as vertical trusses in which the axes of the members are aligned concentrically at the joints. Although the global geometric configuration of a BRBF is very similar to a conventional concentrically braced frame (CBF), the members, connections, and behavior of BRBFs are distinctly different from those of ordinary concentrically braced frames (OCBFs) and special concentrically braced frames (SCBFs). The key difference is the use and behavior of the buckling-restrained brace (BRB) itself. (p. 1)

The following quote is from the government website for the National Institute of Standards and Technology (NIST, 2015).

As the name states, the BRB assembly restrains core buckling under compressive loading and achieves a compressive yield strength that is approximately equal to its tensile yield strength. Therefore, the core area can be sized for design-level seismic loads based on the yield stress of the core,  $F_{y,sc}$ , as opposed to braces in conventional CBFs, which are sized based on the critical buckling stress,  $F_{cr}$ , of the section. Buckling braces in OCBFs and SCBFs have significant excess tensile capacity, and the brace buckling behavior leads to degrading cyclic response. In contrast, as shown in Figure 2, a BRB yields axially in tension and in compression, exhibiting nominally symmetric cyclic response with strain hardening. In BRBFs, the primary source of ductility is the axial yielding of the BRB cores. Unlike BRBFs, CBFs are subject to buckling of the braces and therefore are less ductile. (p. 2)

## Case Study Building

A 40-story, buckling restraint-braced frame structure was selected for this current study. This structure was also used by the Pacific Earthquake Engineering Research Center

(PEER) Tall Buildings Initiative in their case studies (PEER, 2011). Figure 3 shows that the footprint of the above-ground structure was 170' x 107'. It also shows the location of the buckling-restrained chevron braces. Figure 4 shows that the building consisted of four basement levels. The footprint of the basement level was 227' x 220'. Lateral forces were entirely resisted by buckling-restraint braces. Above-grade floors were comprised of 6.25" lightweight concrete fill on metal deck. "Gravity framing consisted of steel column and beams with composite metal deck and lightweight concrete fill. Beams utilized in the BRB bays were designed to remain linear when yielding of the braces occurs under lateral displacements. Columns in the lateral load carrying system were concrete filled steel box columns, fabricated from steel plates (1.5 in. to 3 in.), utilizing continuous welds and filled with high strength concrete" (PEER, 2011).

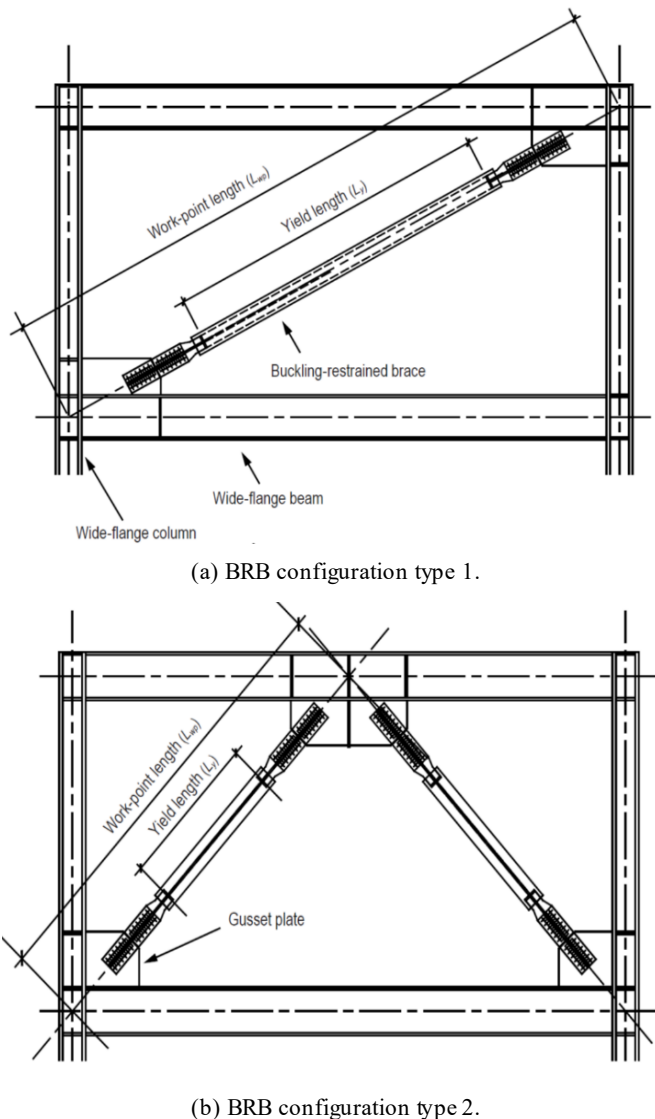


Figure 1. Typical BRBF configurations (NIST, 2015).

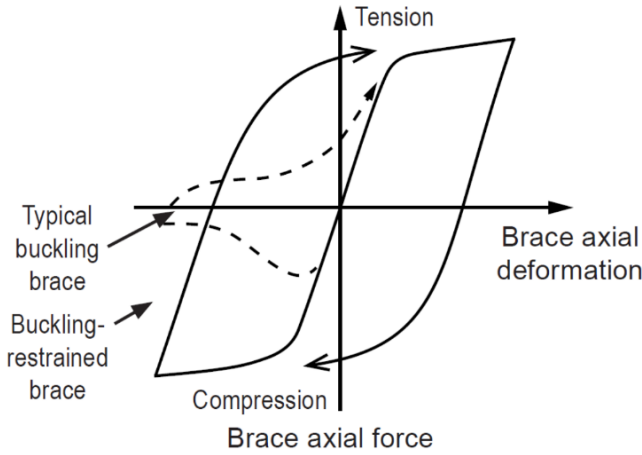


Figure 2. Buckling versus buckling-restrained brace behavior (NIST, 2015).

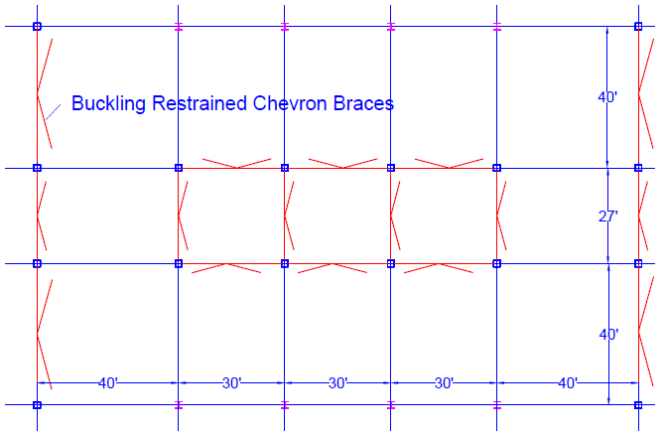


Figure 3. Typical plan view of the BRB building (above ground) [PEER, 2011].

### Seismic Loading and Modeling Procedures

The case study building was located in Los Angeles. Site-specific response spectra and a set of seven pairs of response-spectrum compatible ground motions were provided by Dr. Tony Yang, Prof. Stephen Mahin, and Dr. Yousef Bozorgnia via email on August 3, 2009. The same spectra and spectrum-compatible ground motions have been used in the PEER Tall building initiative for analyzing tall concrete buildings. Figure 5 shows how the actual recorded earthquake time histories were used and modified in the frequency domain in order to match the target spectrum.

PERFORM 3D (CSI, 2006) was used to develop a detailed non-linear model for the numerical analyses in this current study. For detailed modeling descriptions of each component, refer to PEER (2011). Perimeter shear walls (see again Figure 4) were modeled with elastic wall elements with 50% of the gross stiffness and 40% of elastic shear modulus to account for cracked section properties.

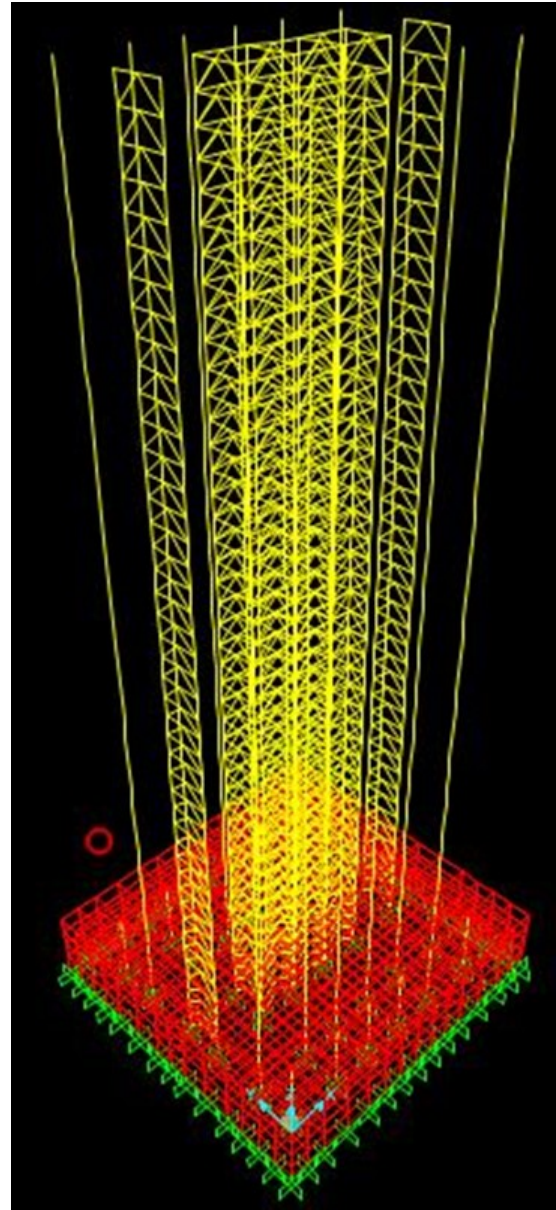


Figure 4. Three-dimensional rendering of the 40-story, BRB structure from PERFORM-3D model.

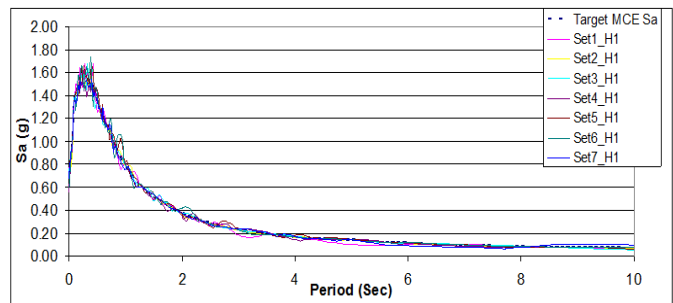


Figure 5. Site-specific response spectrum and seven pairs of spectrum compatible ground.

### BRB Bay Model

The following quote is from the government website, the Pacific Earthquake Engineering Research Center (PEER) (2011).

A typical BRB bay considering any of the structures is made up of concrete box columns, W section steel beams, gusset connections, and BRB members. The modeling strategy to account for all of these elements is shown in Figure 6. All of the elements were modeled with elastic elements except for the BRB core. Strength sections were employed at critical member locations of beams and columns to ensure elastic behavior. If at any point in an analysis the strength demand exceeded the capacity the analysis stops. (p. 89)

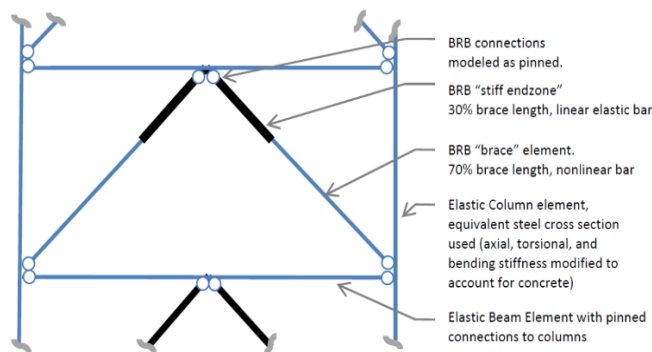


Figure 6. Modeling elements used in a typical BRB bay (PEER, 2015).

The details and assumptions used to model the beams and columns of a typical BRB bay were as follows. Again, these quotes come from PEER (2011).

The concrete filled box columns were modeled with linear non-prismatic steel sections. The area, moment of inertia, and torsional properties of the member cross sections were adjusted to account for the additional stiffening due to the presence of the infill concrete. Strength checks were located at member ends to monitor the interaction of axial and moment loading (PMM interaction). (p. 89)

Beams were modeled with linear, prismatic, standard steel sections. Their stiffness and strength were not adjusted to take into account the presence of the floor slab. Each beam was assumed to span the center-line to center-line distance between the nodes and does not account for the column depth (such as with a rigid beam end zone). In addition, the beams are assumed to be pinned at their ends; therefore, the geometry of the beam-stub, addition-

al bending resistance of the gusset plate, and the partially rigid behavior of the connection were not accounted for. Strength checks for moment capacity were employed at the center of the beams span. (p. 89-90)

The buckling-restrained braces were the only non-linear elements employed in the model, using the built-in BRB component of Perform-3D, a compound bar-type element that resists axial force only and has no resistance to torsional or bending forces (CSI, 2006). The element may be thought of as two bars in series: a linear one to represent end zone behavior and a nonlinear one to represent behavior of the yielding portion of the brace. The following are details and assumptions used in the BRB end zone and brace modeling. (p. 90)

30% of the node-to-node length of the brace element was assigned as a non-yielding end zone. This linear bar represents the combined stiffness of the gusset, the brace connection, and the portion of the column that was not accounted for using center-line to center-line geometry. The strength or stability of the connections was not considered. In essence, it was assumed that they were well designed and would not fail, even under large cyclic displacements. The stiffness of the linear bar was assumed to be much stiffer than the BRB element and was essentially rigid. (p. 90)

70% of the node-to-node length of the brace element was assigned as the nonlinear BRB element. Figure 7 shows the backbone curve of BRBs in terms of force and displacement, and the values that were used to generate it. The analysis stops if the mean strain in any brace exceeds  $20\Delta_y$ , the theoretical ultimate strain limit. In addition, the mean strain in the cores of BRBs were monitored to check that it did not exceed a performance limit of  $0.013 (10\Delta_y)$ , the assumption employed by SCH's design team based on test results conducted at the University of Utah by Romero and Reaveley (Dutta & Hamburger, 2010). For simplicity, isotropic hardening and accumulated deformation capacities were ignored in the BRB model. (p. 90)

Two detailed 3D models of the entire building were developed: 1) a rigid-diaphragm model and 2) a flexible-diaphragm model. Modeling of all the elements was same for both models, with the exception of the floor plates. Following two paragraphs describe the difference between the two models:

### Rigid Diaphragm Model

When high-rise buildings are modeled for non-linear, time-history analyses (NLTHA), most of the engineering

community uses a rigid-diaphragm constraint for all of the floor plates, with the exception of a few special floors—ground floor, below-ground parking floors, and mechanical floors. This current study followed a similar path. The ground floor, parking floors, and mechanical floors were modeled as flexible, using shell elements, while the rest of the floors were modeled as rigid. “Effective thickness comprising of the total thickness of the topping plus half the rib thickness was used. Thus the ground floor was modeled as 10.5 in. thick slab as it represents a 9 in. topping and 1.5 in. half rib height” (PEER, 2011).

### Flexible Diaphragm Model

Each floor of the building was modeled using shell elements. Elastic shell elements were used with 30% of the gross cross-sectional properties.

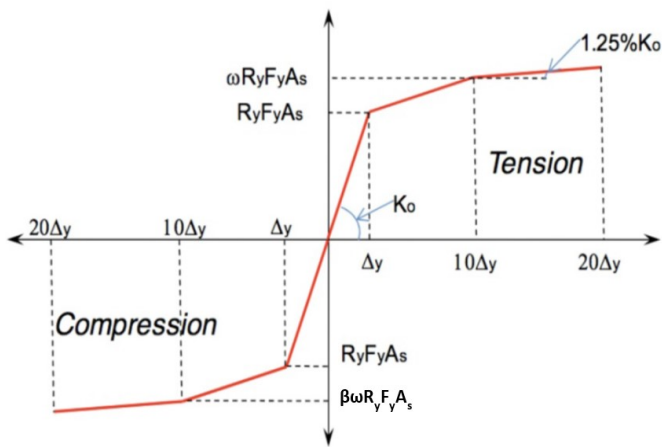


Figure 7. General backbone curve for the nonlinear BRB element. The vertical axis represents force and the horizontal axis represents deformation.  $A_s$  = area of yielding steel core,  $K_0 = A_s/L$ ,  $E = 29000$  ksi,  $F_y = 38$  ksi,  $R_y = 1.1$ ,  $\omega = 1.25$ ,  $\beta = 1.1$ , and  $L = 70\%$  of the brace length (using center-line to center-line geometry) [PEER, 2015].

## Results

Table 1 shows a comparison of the modal periods of the structure with rigid and flexible diaphragms. It also shows that torsional modal period was 4.761 seconds for the flexible diaphragm compared to 4.512 seconds for the rigid diaphragm (5.5% increase). In the UX direction, a period of 3.951 seconds was observed for the flexible diaphragm compared to 3.782 seconds for the rigid diaphragm (4.5% increase). 3D, non-linear, time-history analyses were performed using seven sets of ground motions for the two models. The author found that, for each NLTHA for the flexible-diaphragm model, it took several days to complete and a huge amount of hard-drive space. Figures 8-14 summarize the results of the analyses and show a comparison between the flexible-diaphragm and rigid-diaphragm models for the case study building.

Table 1. Comparison of modal periods.

	Flexible Diaphragm (seconds)	Rigid Diaphragm (seconds)
Model 1	6.071 (UY)	5.983 (UY)
Model 2	4.761 (Torsion)	4.515 (Torsion)
Model 3	3.951 (UX)	3.782 (UX)
Model 4	1.719 (UY)	1.653 (UY)
Model 5	1.548 (Torsion)	1.455 (Torsion)
Model 6	1.353 (UX)	1.276 (UX)

For the flexible-diaphragm model, seven analyses were performed. Figures 8-12 show the outputs from each of the analyses (represented using a thin solid line). As expected, variability in the response for each earthquake’s ground motions is evident from the scatter of thin lines. The average of the seven responses is represented with a bold solid line in Figures 8 to 12. Similarly in Figures 8-12, thin dotted lines represent results from the rigid-diaphragm model, and bold dotted lines represent the average of the seven. Figure 8 shows a comparison of the results of floor acceleration; if averages of the response were compared, it could be seen that the bold solid line would be further away from the bold dotted line. This is true for a most all of the story levels.

Even if individual ground motions were compared, significantly higher levels of acceleration for the flexible diaphragm would be shown. Periods of vibration for the flexible-diaphragm model were higher (see again Table 1), and a higher mode-acceleration response might cause the flexible-diaphragm model to yield higher accelerations in each floor of the building. Figures 9 and 10 show comparisons of floor displacement and inter-story drift, respectively. The figures also show a slight increase in displacement and inter-story drift for the flexible diaphragm. Figures 11 and 12 show comparisons of story shear and story moment, respectively. Negligible differences were observed from the figures. Demand-capacity ratio (DCR) of BRBs is one of the most important design and non-linear assessment considerations.

Figures 13 and 14 show the differences in response, in percentage (%), for BRBs for Line 3 and Line 4 elements, respectively. The positive numbers in both of the figures indicate that response for the flexible-diaphragm model was higher. Observation indicated a 5%-10% increase in DCR for middle half-floors of the buildings. Even though there were some negative numbers (indicating higher DCRs for the rigid diaphragm), the original DCRs were not that high. For example, BRBs in this region of the building were: DCR for the flexible diaphragm was 0.29 compared to a DCR for the rigid diaphragm was 0.3.

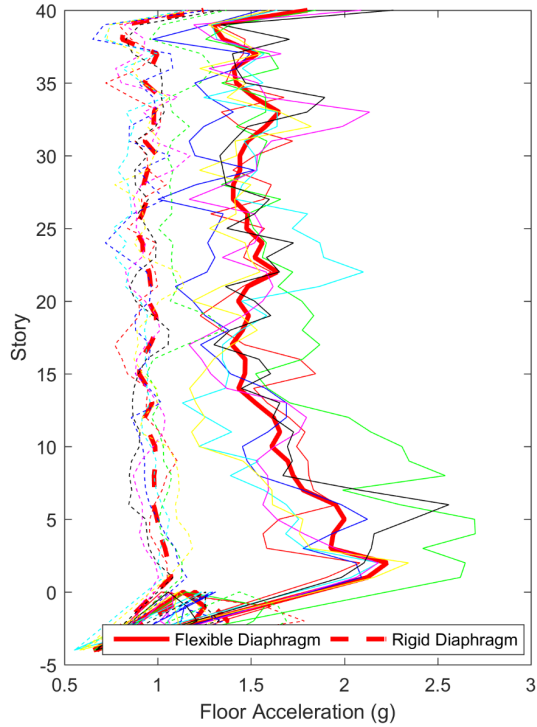


Figure 8. Comparison of floor acceleration (X-direction). Solid lines for the flexible diaphragm; dotted lines for the rigid diaphragm; bold lines for response averages.

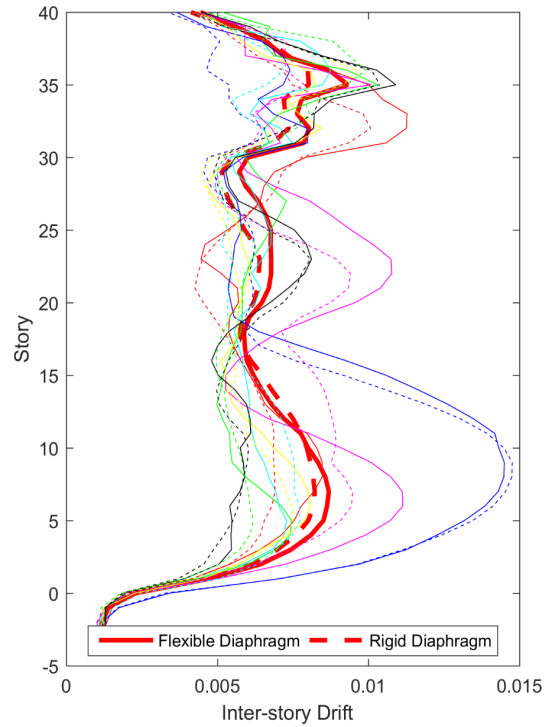


Figure 10. Comparison of Inter-story drift (X-direction). Solid lines for the flexible diaphragm; dotted lines for the rigid diaphragm; bold lines for response averages.

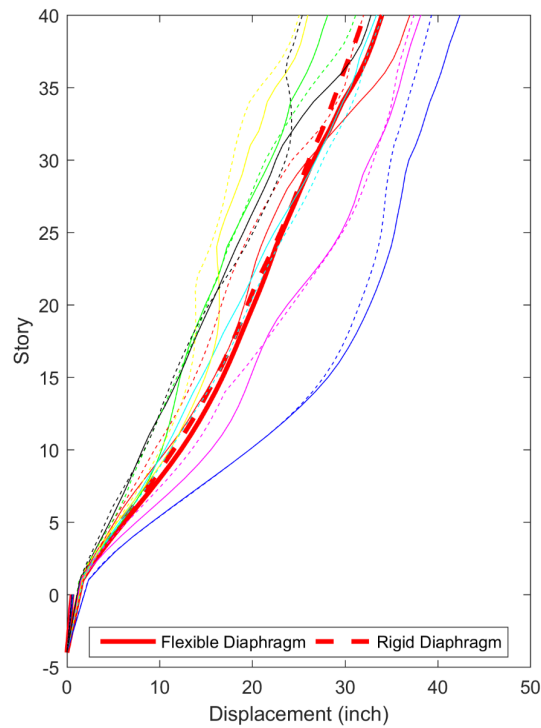


Figure 9. Comparison of Floor displacement (X-direction). Solid lines for the flexible diaphragm; dotted lines for the rigid diaphragm; bold lines for response averages.

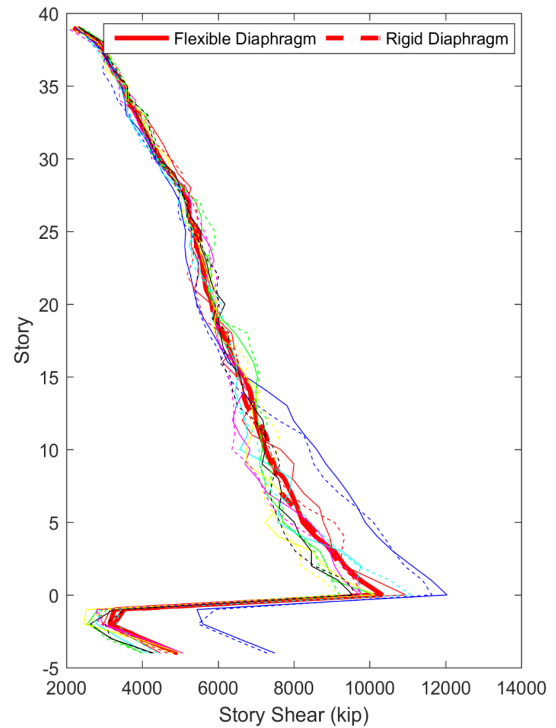


Figure 11. Comparison of Story Shear (X-direction). Solid lines for the flexible diaphragm; dotted lines for the rigid diaphragm; bold lines for response averages.

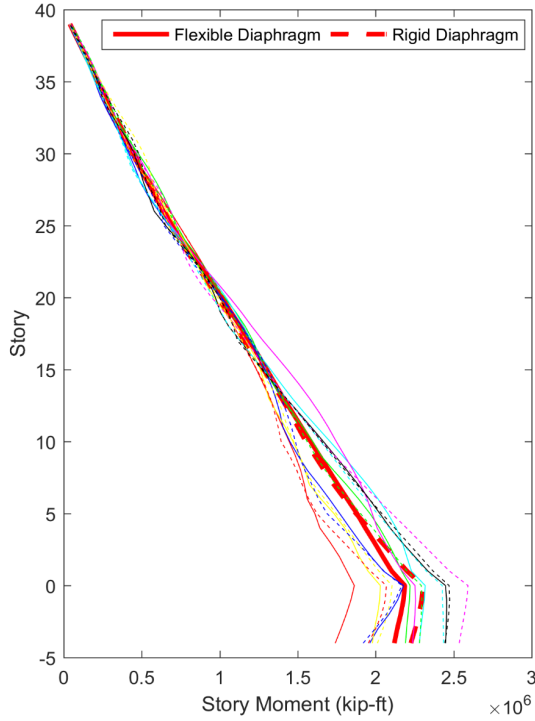


Figure 12. Comparison of Story Moment (Y-direction). Solid lines for the flexible diaphragm; dotted lines for the rigid diaphragm; bold lines for response averages.

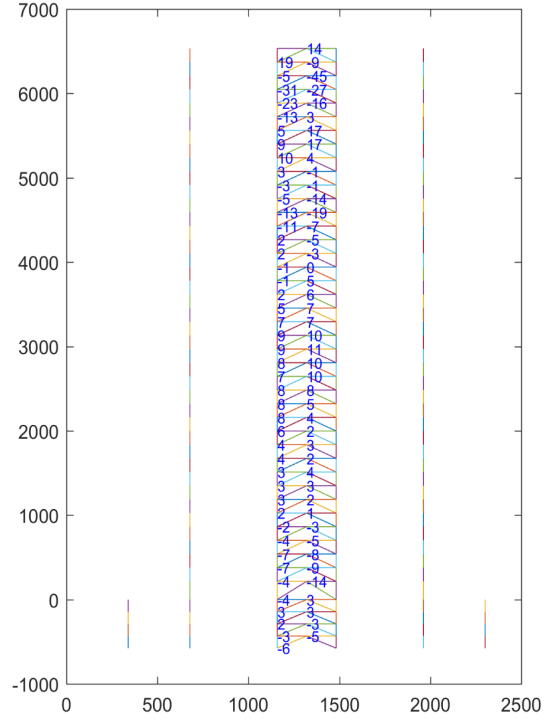


Figure 14. Difference in response in percentage (%): demand-capacity-ratio (DCR) of BRBs (Line 4 elements are shown in the figure).

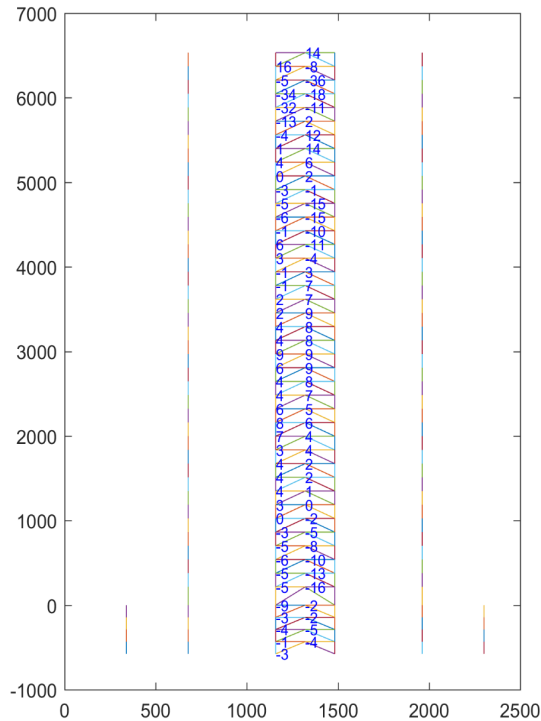


Figure 13. Difference in response in percentage (%): demand-capacity-ratio (DCR) of BRBs (Line 3 elements are shown in the figure).

## Conclusions

A 40-story, buckling restraint-braced framed building was analyzed and modeled for seven pairs of ground motion for flexible-diaphragm and rigid-diaphragm model in order to find out the differences in response. Modal analysis indicated an increase in period of vibration for the flexible-diaphragm model. Also observed for the flexible-diaphragm model were significantly higher levels of floor acceleration and a slight increase in displacement and inter-story drift response. In terms of story shear and story moment, the differences were negligible between the flexible- and rigid-diaphragm models. Also, slight increases in DCRs of BRBs were noticed for the middle portion of the building for the flexible-diaphragm model. Future studies should include tall concrete buildings with different framing systems and steel structures with other framing systems.

## References

- Barron, J., & Hueste, M. (2004). Diaphragm effects in rectangular reinforced concrete buildings. *ACI Structural Journal*, 101(5), 615-624.
- Basu, D., & Jain, S. (2004). Seismic Analysis of Asymmetric building with flexible floor diaphragms. *Journal of Structural Engineering*, 130(8), 1169-1176.
- Bhuiyan, M., & Leon, R. (2013, May). *Effect of diaphragm flexibility on Tall building responses*. Paper presented

- 
- at the ASCE/SEI Structures Congress, Pittsburgh, PA, USA.
- Computers and Structures, Inc. (2006). PERFORM-3D – Nonlinear Analysis and Performance Assessment for 3D Structures [Computer software]. Computers and Structures, Inc., Berkeley, California.
- Dutta, A., & Hamburger, R. (2010). Case study of a 40-story buckling-restrained braced frame building located in Los Angeles. *The Structural Design of Tall and Special Buildings*, 19(1-2), 77-93.
- Fang, C. (2015). *The Seismic Behavior of Steel Structures with Semi-Rigid Diaphragms* (Unpublished doctoral dissertation). Virginia Polytechnic Institute and State University, Blacksburg, Virginia, USA.
- National Institute of Standards and Technology (NIST). (2015). *Seismic Design of Steel Buckling-Restrained Braced Frames* (Report No. NIST GCR 15-917-34). NEHRP Seismic Design Technical Brief No. 11, NIST, Gaithersburg, MD.
- Pacific Earthquake Engineering Research Center (PEER). (2011). *Case Studies of the Seismic Performance of Tall Buildings Designed by Alternative Means* (Report No. PEER 2011/05). Pacific Earthquake Engineering Research Center, Berkeley, California.
- Tena-Colunga, A., & Abrams, P. (1996). Seismic behavior of structures with flexible diaphragms. *Journal of Structural Engineering*, 122(4), 439-445.

## Biographies

**MOHAMMAD T. BHUIYAN** is an Associate Professor of Civil Engineering at West Virginia State University. He earned his BSc in Civil Engineering from Bangladesh University of Engineering and Technology, Dhaka; MSc in Earthquake Engineering jointly from Universite Joseph Fourier, France, and ROSE School, Italy; and, PhD in Earthquake Engineering from ROSE School with a joint program at Georgia Tech. His research interests include tall buildings, earthquake engineering, and soil-structure interaction. Dr. Bhuiyan may be reached at [towhid@wvstateu.edu](mailto:towhid@wvstateu.edu)

# INSTRUCTIONS FOR AUTHORS: MANUSCRIPT FORMATTING REQUIREMENTS

The INTERNATIONAL JOURNAL OF ENGINEERING RESEARCH AND INNOVATION is an online/print publication designed for Engineering, Engineering Technology, and Industrial Technology professionals. All submissions to this journal, submission of manuscripts, peer-reviews of submitted documents, requested editing changes, notification of acceptance or rejection, and final publication of accepted manuscripts will be handled electronically. The only exception is the submission of separate high-quality image files that are too large to send electronically.

All manuscript submissions must be prepared in Microsoft Word (.doc or .docx) and contain all figures, images and/or pictures embedded where you want them and appropriately captioned. Also included here is a summary of the formatting instructions. You should, however, review the [sample Word document](http://ijeri.org/formatting-guidelines) on our website (<http://ijeri.org/formatting-guidelines>) for details on how to correctly format your manuscript. The editorial staff reserves the right to edit and reformat any submitted document in order to meet publication standards of the journal.

The references included in the References section of your manuscript must follow APA-formatting guidelines. In order to help you, the sample Word document also includes numerous examples of how to format a variety of scenarios. Keep in mind that an incorrectly formatted manuscript will be returned to you, a delay that may cause it (if accepted) to be moved to a subsequent issue of the journal.

1. **Word Document Page Setup:** Two columns with ¼" spacing between columns; top of page = ¾"; bottom of page = 1" (from the top of the footer to bottom of page); left margin = ¾"; right margin = ¾".
2. **Paper Title:** Centered at the top of the first page with a 22-point Times New Roman (Bold), small-caps font.
3. **Page Breaks:** Do not use page breaks.
4. **Figures, Tables, and Equations:** All figures, tables, and equations must be placed immediately after the first paragraph in which they are introduced. And, each must be introduced. For example: "Figure 1 shows the operation of supercapacitors." "The speed of light can be determined using Equation 4:"

5. **More on Tables and Figures:** Center table captions above each table; center figure captions below each figure. Use 9-point Times New Roman (TNR) font. Italicize the words for table and figure, as well as their respective numbers; the remaining information in the caption is not italicized and followed by a period—e.g., "*Table 1*. Number of research universities in the state." or "*Figure 5*. Cross-sectional aerial map of the forested area."
6. **Figures with Multiple Images:** If any given figure includes multiple images, do NOT group them; they must be placed individually and have individual minor captions using, "(a)" "(b)" etc. Again, use 9-point TNR.
7. **Equations:** Each equation must be numbered, placed in numerical order within the document, and introduced—as noted in item #4.
8. **Tables, Graphs, and Flowcharts:** All tables, graphs, and flowcharts must be created directly in Word; tables must be enclosed on all sides. The use of color and/or highlighting is acceptable and encouraged, if it provides clarity for the reader.
9. **Textboxes:** Do not use text boxes anywhere in the document. For example, table/figure captions must be regular text and not attached in any way to their tables or images.
10. **Body Fonts:** Use 10-point TNR for body text throughout (1/8" paragraph indentation); indent all new paragraphs as per the images shown below; do not use tabs anywhere in the document; 9-point TNR for author names/affiliations under the paper title; 16-point TNR for major section titles; 14-point TNR for minor section titles.



11. **Personal Pronouns:** Do not use personal pronouns (e.g., "we" "our" etc.).
12. **Section Numbering:** Do not use section numbering of any kind.
13. **Headers and Footers:** Do not use either.

- 
14. **References in the Abstract:** Do NOT include any references in the Abstract.
  15. **In-Text Referencing:** For the first occurrence of a given reference, list all authors—last names only—up to seven (7); if more than seven, use “et al.” after the seventh author. For a second citation of the same reference—assuming that it has three or more authors—add “et al.” after the third author. Again, see the *sample Word document* and the *formatting guide for references* for specifics.
  16. **More on In-Text References:** If you include a reference on any table, figure, or equation that was not created or originally published by one or more authors on your manuscript, you may not republish it without the expressed, written consent of the publishing author(s). The same holds true for name-brand products.
  17. **End-of-Document References Section:** List all references in alphabetical order using the last name of the first author—last name first, followed by a comma and the author’s initials. Do not use retrieval dates for websites.
  18. **Author Biographies:** Include biographies and current email addresses for each author at the end of the document.
  19. **Page Limit:** Manuscripts should not be more than 15 pages (single-spaced, 2-column format, 10-point TNR font).
  20. **Page Numbering:** Do not use page numbers.
  21. **Publication Charges:** Manuscripts accepted for publication are subject to mandatory publication charges.
  22. **Copyright Agreement:** A copyright transfer agreement form must be signed by all authors on a given manuscript and submitted by the corresponding author before that manuscript will be published. Two versions of the form will be sent with your manuscript’s acceptance email.
  23. **Submissions:** All manuscripts and required files and forms must be submitted electronically to Dr. Philip D. Weinsier, manuscript editor, at [philipw@bgsu.edu](mailto:philipw@bgsu.edu).
  24. **Published Deadlines:** Manuscripts may be submitted at any time during the year, irrespective of published deadlines, and the editor will automatically have your manuscript reviewed for the next-available issue of the journal. Published deadlines are intended as “target” dates for submitting new manuscripts as well as revised documents. Assuming that all other submission conditions have been met, and that there is space available in the associated issue, your manuscript will be published in that issue if the submission process—including payment of publication fees—has been completed by the posted deadline for that issue.

Missing a deadline generally only means that your manuscript may be held for a subsequent issue of the journal. However, conditions exist under which a given manuscript may be rejected. Always check with the editor to be sure. Also, if you do not complete the submission process (including all required revisions) within 12 months of the original submission of your manuscript, your manuscript may be rejected or it may have to begin the entire review process anew.

**Only one form is required. Do not submit both forms!**

The form named “paper” must be hand-signed by each author. The other form, “electronic,” does not require hand signatures and may be filled out by the corresponding author, as long as he/she receives written permission from all authors to have him/her sign on their behalf.

The *International Journal of Engineering Research & Innovation (IJERI)* is a highly-selective, peer-reviewed print journal which publishes top-level work from all areas of engineering research, innovation and entrepreneurship.

## **IJERI Contact Information**

General questions or inquiries about sponsorship of the journal should be directed to:

Mark Rajai, Ph.D.

Founder and Editor-In-Chief

Office: (818) 677-5003

Email: [editor@ijeri.org](mailto:editor@ijeri.org)

Department of Manufacturing Systems Engineering & Management

California State University-Northridge

18111 Nordhoff St.

Room: JD3317

Northridge, CA 91330